

Emergence of Surface-Enhanced Raman Scattering Probes in Near-Infrared Windows for Biosensing and Bioimaging

Hui Chen,[‡] Ziyi Cheng,[‡] Xuejun Zhou, Rui Wang,^{*} and Fabiao Yu^{*}



Cite This: *Anal. Chem.* 2022, 94, 143–164



Read Online

ACCESS |

Metrics & More

Article Recommendations

CONTENTS

1. Rational Design of NIR SERS for Sensitive Detection	145
1.1. CCD Detector	145
1.2. Rational Design of SERS Probe	145
1.2.1. SERS Substrates	145
1.2.2. Raman Reporter Molecules	148
1.2.3. Capsulation	149
2. Biosensing and Bioimaging in the NIR Biological Window	150
2.1. Nucleic Acid	150
2.2. Proteins and Small Biological Molecules	152
2.3. Dynamic SERS Sensing of Biological Environment	154
2.4. Pathogens Identification	154
2.5. NIR SERS Bioimaging	155
3. Therapy Based on NIR SERS Probes	156
3.1. Photothermal Therapy	156
3.1.1. Photothermal Tumor Cell Eradication	156
3.1.2. Photothermal Antimicrobial Therapy	157
3.2. Therapeutic Drug Delivery System	158
3.3. SERS Image-Guided Surgery Therapy	159
4. Summary and Perspective	160
Author Information	160
Corresponding Authors	160
Authors	160
Author Contributions	161
Notes	161
Biographies	161
Acknowledgments	161
References	161

The abnormal fluctuations of various biomarkers (such as intracellular nucleic acid, lipid, protein, pH, etc.) can be used as valuable diagnostic indicators for monitoring the physiological and pathological processes.^{1–4} Traditional detection and imaging methods often face various deficiencies and new challenges. Thus, sensing and imaging techniques with properties such as having no contact, being in real-time, and having deep tissue penetration and high spatial resolution are urgently needed, which can display intrinsic chemical components in tissues and provide useful information for biomedical applications. In the past decades, surface-enhanced Raman scattering (SERS) has received more and more attention

owing to its ultrahigh sensitivity and noninvasiveness.^{5–7} As a powerful vibrational spectroscopic technique, SERS can provide useful information about the chemical structure and surrounding environment with an enhancement of up to single molecule level. Also, with a very narrow peak width, usually a few tenths of the fluorescence peak width, SERS makes multiplexing target detection in single excitation light possible.^{8,9} In 1974, the SERS phenomenon was first discovered by Fleischmann and his colleagues when observing the Raman spectrum of pyridine molecules adsorbed on the surface of a rough silver electrode. During this process, the intensity of the Raman spectrum of the pyridine molecule on the electrode surface has been significantly improved compared to before. Moreover, the phenomenon has been developed as technique to detect the substances by identifying their specific Raman peaks, which has attracted extensive attention due to the greatly enhanced Raman signal of analyte. The mechanism of SERS signal enhancement mainly comes from two main theoretical mechanisms: electromagnetic enhancement (EM) and chemical enhancement (CE).⁹ The coupling of localized surface plasmon resonance (LSPR) with incident light produces a secondary electric field around the plasmonic nanostructure, resulting in “hot spot”, which is related to the composite, shape and size of the nanostructure. The molecule near or adsorbed on the metal surface will experience greatly enhanced Raman signal intensity. EM mode doesn't exhibit chemical-selectivity, providing the same enhancement for any type of molecule, which is distance-dependent. Only the molecule on or very close to the metal surface, the strong enhancement can be obtained. Since EM enhancement can't explain all the SERS phenomenon, the researchers then propose the CE mechanism. CE is acquired by enlarging the scattering cross-section of Raman reporters, which are grafted onto the plasmonic nanoparticles (NPs) with stable chemical bonds to generate SERS fingerprint signatures, and accounts for an enhancement up to two orders of magnitude. Therefore, the degree of enhancement depends on the metal substrate's electromagnetic properties and the Raman reporters' chemical properties.

Special Issue: Fundamental and Applied Reviews in Analytical Chemistry 2022

Published: November 23, 2021



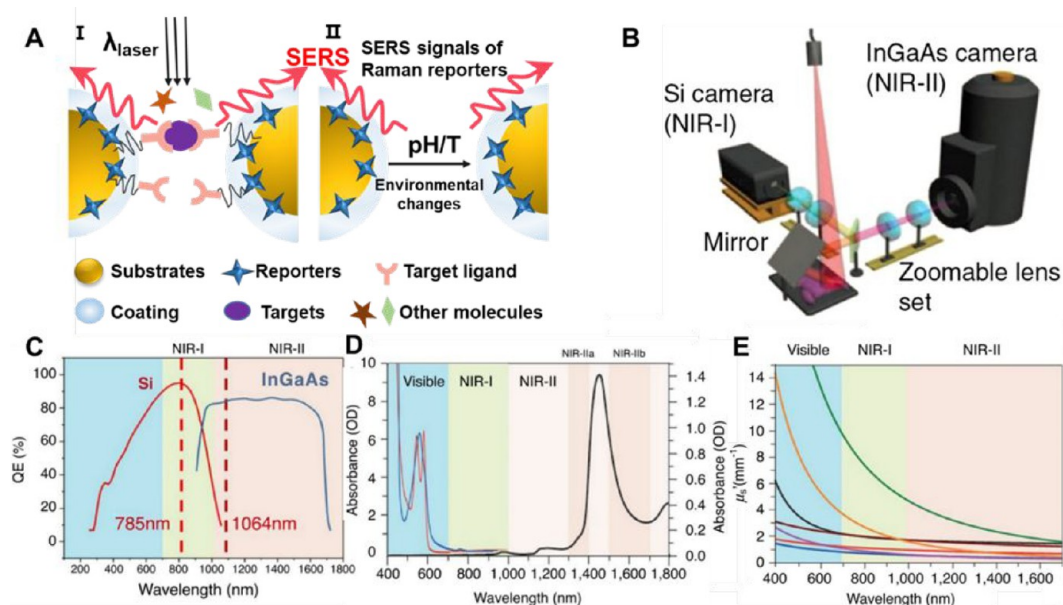


Figure 1. (A) Schematic diagram of indirect SERS detection: (i) the biocompatible SERS nanoprobe combines reporter molecules on the substrate surface, binding targeted ligands under the protection of the peripheral coating. When the target molecule appears near the hot spot generated between two metal substrates, a significantly enhanced SERS signal can be obtained. (ii) When the reaction system environment changes, such as pH or temperature changes, the SERS signal of the reporter molecule will change. (B) A schematic of the imaging setup for the simultaneous detection of both NIR-I and NIR-II photons using Si and InGaAs cameras (Reprinted from *Adv. Drug Delivery Rev.*, Vol. 65, Gong, H.; Peng, R.; Liu, Z. Carbon nanotubes for biomedical imaging: The recent advances, pp. 1951–1963 (ref 16). Copyright 2013, with permission from Elsevier.). (C) Sensitivity curves for typical cameras based on Si or InGaAs, which are sensitive in the first and second near-infrared windows, respectively. The excitation wavelengths at 785 and 1064 nm are indicated by vertical dotted lines. (D) Absorbance of oxygenated (red curve) and deoxygenated (blue curve) hemoglobin in the visible and NIR spectrum, together with water absorbance (black curve) at 1400–1500 nm. (E) Plots of the scattering attenuation coefficient as a function of wavelength for various *ex vivo* tissues (from top to bottom: green curve = brain tissue, yellow curve = intralipid tissue phantom, black curve = skin, brown curve = cranial bone, purple curve = mucous tissue, red curve = subcutaneous tissue, and blue curve = muscle tissue) (Reprinted from *Curr. Opin. Chem. Biol.*, Vol. 45, Lane, L. A.; Xue, R.; Nie, S. Emergence of two near-infrared windows for *in vivo* and intraoperative SERS, pp. 95–103 (ref 14). Copyright 2018, with permission from Elsevier.).

Typical SERS detection can be simply divided into two types, namely, direct detection without labels and an indirect method based on SERS labels.^{7,10–12} The traditional SERS-based label-free detection can be realized through the direct interactions between the targets and the SERS-based nanostructure to obtain the vibrational spectrum information on the targets, which is limited to the complicated signal assignment, poor throughput, and limited sensitivity.^{7,10} Indirect detection usually uses Raman reporter molecules to label the SERS substrates and results in a strong SERS signal for analyte measurements, which enables the deficiencies encountered in the direct detection to be overcome. The labeled SERS detection can obtain the intrinsic fingerprint signal of specific Raman reporter molecules, which significantly improves the stability of SERS probes and allows highly reproducible quantitative analysis of biomolecules *in vitro* and *in vivo* (Figure 1A).

When applied on active biosensor platform, the selection of NIR window for SERS detection shows many advantages: (i) deep tissue penetration due to negligible absorption and low scattering in NIR; (ii) less tissue interference spontaneous fluorescence; (iii) minimal tissue damage. Based on the quenching ability of metal substrate to fluorophore, the quench chromophore contains a close energy to the NIR exciting radiation, which was widely used as Raman reporters. Substrates with different morphologies were used to explore sensitive SERS detection in the NIR region. Many impressive developments have been achieved on NIR SERS and its biomedical applications; however, before NIR SERS is applied to practical

clinical diagnosis, much effort is needed to improve the reliability and sensitivity of SERS detection in biological systems. SERS addresses the following key problems that other bioanalytical techniques cannot solve: (1) Low detector efficiency in the NIR region and high cost of the detector in the NIR II region; (2) Difficulty in the design of nanostructures with high SERS activity; (3) Less Raman reporter molecules in the NIR region, especially in the NIR II region. Common SERS detection usually uses laser in the wavelength range of the visible region (400–650 nm) as the excitation light. When applied to biological tissues, it produces a large amount of photon scattering and absorption, resulting in limited tissue penetration depth and significant interference from the tissue's autofluorescence.^{13,14} In order to overcome these difficulties, near-infrared (NIR) light in the two biological windows has gained much more interest for biosensing and *in vivo* imaging. NIR light can penetrate deep biological tissues compared to visible light owing to the less scattering and absorption at the longer wavelength light for the tissues. The NIR window has been further divided into two regions, categorized as the first (650–900 nm) and the second (1000–1700 nm) NIR window.¹⁵ An accurate signal comes from the efficient charge-coupled device (CCD) detector. Within the spectral range of 900 nm, it is mainly defined by the silicon (Si) CCD detector, but its detection efficiency drops after 900 nm. Since the quantum efficiency of the indium gallium arsenide (InGaAs) detector begins to increase dramatically after 1000 nm, the spectral boundary larger than 1000 nm is mainly defined by the InGaAs

detector, both of which have low quantum efficiency in the range of 900–1000 nm (Figure 1B,C).¹⁶ Additionally, the selection of the NIR window for SERS detection shows many advantages: (i) deep tissue penetration due to negligible absorption and low scattering in NIR; (ii) less tissue interference of spontaneous fluorescence; (iii) minimal tissue damage (Figure 1D,E).^{16,17} These integrated advantages are suitable for biosensing and bioimaging in preclinical and clinical applications. Thus, when the SERS probe is applied on the active biosensor platform, it should be committed to using NIR light for excitation and a low power value to prevent the possible damage of living cells and minimize the time of signal accumulation, so as to obtain accurate information on the dynamic physiological and pathological process of living cells.

Herein, we focus on reviewing the most recent advances of the NIR SERS probe in biosensing and bioimaging applications. To guide the reader to better understand NIR SERS and its factors that may interfere with the highly sensitive detection in biomedical applications, we first propose the key challenges to perform highly sensitive NIR SERS measurement including the CCD detector and the design of active NIR SERS probes. Thereafter, we introduce the fundamental design principle of NIR SERS for highly sensitive detection, covering active NIR SERS substrates, NIR Raman reporter molecules, and surface encapsulation. Recently developed biosensing and bioimaging strategies in the NIR biowindow, such as different molecules including nucleic acid, proteins, and small molecules, pathogens, various biological processes, etc., are systematically reviewed. Through the innovative fabrication of NIR-active SERS probes and subsequent modification, various SERS imaging-guided therapy platforms are properly designed, demonstrating preferable *in vitro* and *in vivo* therapeutic performance. Finally, we summarize the future challenges and prospects of NIR-active SERS probes in both two near-infrared biowindows. This Review aims to better understand NIR SERS biosensing and bioimaging and motivate their further clinical applications.

1. RATIONAL DESIGN OF NIR SERS FOR SENSITIVE DETECTION

Following the key challenges, we will discuss the CCD detector and the rational principles/strategies to perform highly sensitive NIR SERS detection. As the key component of NIR SERS detection, the development of SERS probe can be considered as a significant step in the biosensing and bioimaging. A typical SERS probe usually comprises four parts: a noble metal nanostructure as substrate for signal enhancement, a Raman reporter molecule, a coating shell for improving biocompatibility and stability of SERS probe, and a biorecognition element such as antibody, aptamer and peptide. The substrate can provide greatly enhanced Raman signals due to the localized surface plasmon resonance on the surface of the metals. The SERS properties of the probe can be greatly affected by the metal core's shape, size, composition and structure. In addition, Raman reporter molecules should be adsorbed on the surface of the substrate to provide fingerprint SERS peaks. To improve the stability and avoid the surrounding interference, a coating shell should be carefully designed. Furthermore, the introduction of targeting molecules is essential to improve the probes' functionality. Thereby, we hope NIR SERS can be utilized as a powerful tool in biomedical applications.

1.1. CCD Detector. In order to ensure highly sensitive SERS detection, first, it is necessary to develop a high-quality CCD to obtain efficient signals. In the range of 900–1000 nm, this area is

not defined and classified by a suitable CCD detector. Also, the laser, detector, and other equipment required by the NIR-II window are more expensive than those required by the NIR-I window; thus, the practical application of the NIR-II window is limited. The requirements of hardware equipment are also an extremely important link in the development of NIR SERS, which ensures probes obtain stable and accurate signals in the detection process.

1.2. Rational Design of SERS Probe. To improve the sensitivity and reproducibility of SERS detection, a reasonable experimental design has been continuously explored, so that NIR SERS can be applied to biological analysis more effectively. It is well-known that the function of SERS is mainly realized through a SERS active probe.^{10,18} Unfortunately, in the application of biology and preclinical and clinical cases, SERS signals are often affected by spontaneous Raman intrinsic signals of samples, self-aggregation, and poor reproducibility. Hence, the ingenious design of the SERS probe is crucial to improve the reproducibility of SERS signals and avoid interference from the samples.¹⁹

Due to the maximization of penetration and minimization of tissue autofluorescence in the NIR, the applications of SERS based on the NIR region in living subjects have great potential. The development of nanostructures that can well match NIR excitation and generate high SERS enhancement at relatively low laser power levels remains an attractive challenge. Most of the NIR active SERS probes have a LSPR occurring in the NIR region. However, it requires a very complex synthesis process to make its LSPR redshift to the NIR region. Therefore, some only use the light excitation in the NIR region, which causes relatively little damage to the tissues or pathogens in the detected area, to assist with other methods such as microfluidic and multimodal methods to improve the detection sensitivity. Although the first biological window provides higher tissue penetration than the visible wavelength, it can be replaced by moving to a longer wavelength in the second NIR window with lower scattering and autofluorescence background, which also demonstrated deeper tissue penetration and a higher maximum permissible exposure in the skin than NIR-I.²⁰ However, due to the limited research progress of the NIR-II substrate, most of the gold nanostructures with absorption peaks in this region are too large to meet effective cell uptake at least in one dimension. At present, most methods etch the edge angle of the substrate by electron displacement, thus affecting the tunability of the plasma band entering the NIR-II region and the corresponding local electromagnetic field amplification.²¹ As a result, the synthesis of the shapes and sizes of these metal structures is a very complex process, and the use of noble metals is inevitably costly. Accordingly, researchers are currently developing novel SERS probes that are active in this area.

1.2.1. SERS Substrates. SERS substrates with good enhancement and stability are the footstone for SERS detection. When the size, shape, and morphology of the SERS substrates are adjusted, tunable longitudinal LSPR can be obtained to realize SERS signal enhancement.^{22,23} When the incident light and molecular scattering signal resonate with the plasmonic frequency, there are many hot spots generated around the plasmonic nanostructure with a maximum SERS signal. Hot spots are known to produce an intense EM field that is generated at the gaps between mild aggregation of the metal. The enhancement factor at the hot spots plays a vital role in the amplification of the Raman signals, which can be enough for the detection of a single molecule.^{20,24}

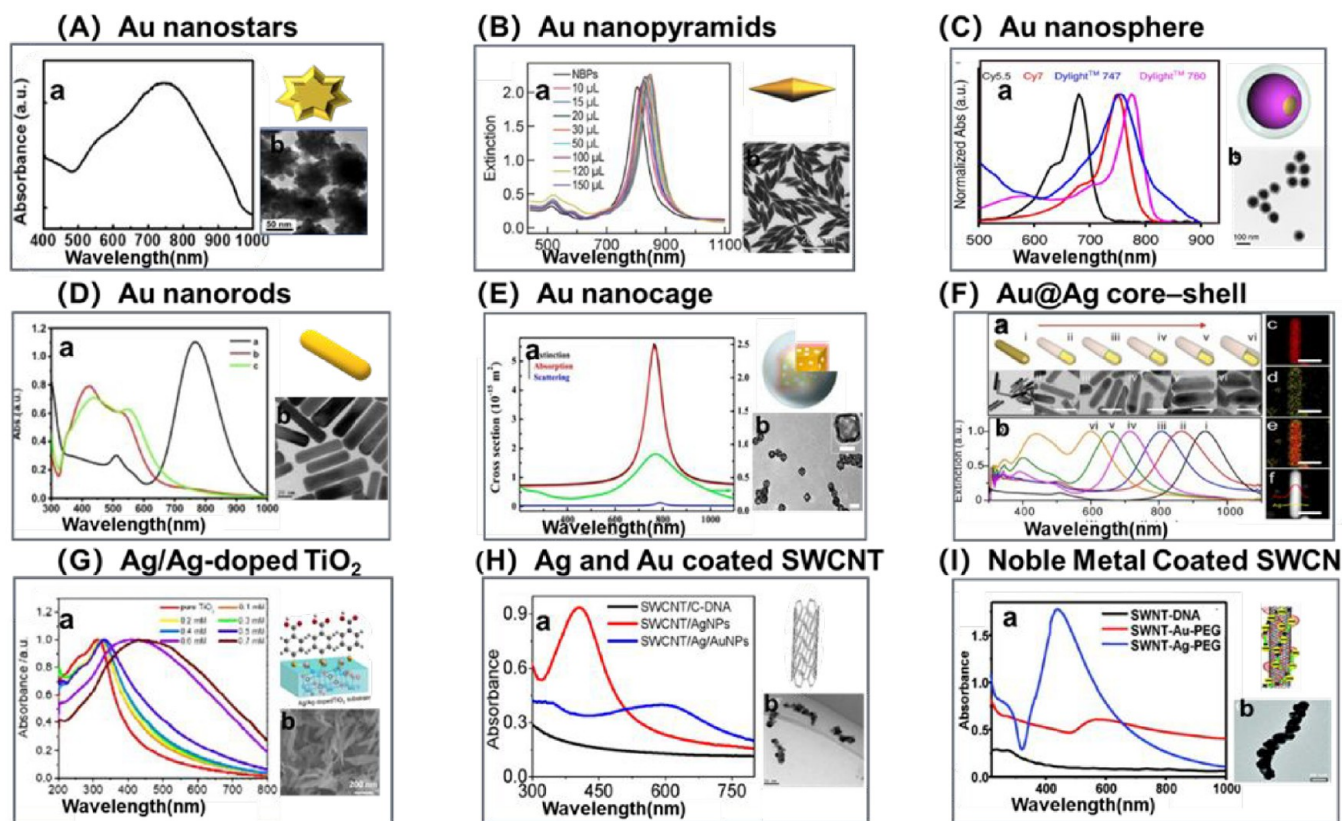


Figure 2. Representative nanosubstrates of NIR active SERS probes. (A-a) UV–vis absorption spectra showing the SPR peak of the gold nanostar at ~ 745 nm. (A-b) Representative SEM image of a gold nanostar (Reproduced from Park, S.; Lee, J.; Ko, H. *ACS Appl. Mater. Interfaces*. 2017, 9, 44088–44095 (ref 26). Copyright 2017 American Chemical Society.). (B-a) Extinction spectra of the Au NBP and Au NBP/mSiO₂ nanostructure samples produced with 10, 15, 20, 30, 50, 100, 120, and 150 μ L of the CTAB solution (0.1 M), respectively. (B-b) Typical TEM images of Au NBPs (scale bar: 200 nm) (Reproduced from Selective Pd Deposition on Au Nanobipyramids and Pd Site-Dependent Plasmonic Photocatalytic Activity, Zhu, X.; Jia, H.; Zhu, X.-M.; Cheng, S.; Zhuo, X.; Qin, F.; Yang, Z.; Wang, J. *Adv. Funct. Mater.*, Vol. 27, Issue 22 (ref 27). Copyright 2017, with permission from Wiley). (C-a) UV–vis NIR spectra of 4 different fluorophores of a modified Au nanosphere. (C-b) Typical TEM images (Reprinted by permission from Macmillan Publishers Ltd.: *Nature Communications*, Pal, S.; Ray, A.; Andreou, C.; Zhou, Y.; Rakshit, T.; Wlodarczyk, M.; Maeda, M.; Toledo-Crow, R.; Berisha, N.; Yang, J.; Hsu, H.-T.; Oseledchik, A.; Mondal, J.; Zou, S.; Kircher, M. F., *Nat. Commun.* 2019, 10, 1926 (ref 28). Copyright 2019, with permission from Springer Nature). (D-a) UV absorption spectra of AuNRs (a), Au@AgNRs (b), and Au@AgNRs@BSA (c). Scale bar = 20 nm. (D-b) Typical TEM images of AuNRs (Reprinted from *Talanta*, Vol. 150, Yue, J.; Liu, Z.; Cai, X.; Ding, X.; Chen, S.; Tao, K.; Zhao, T. Bull serum albumin coated Au@Agnanorods as SERS probes for ultrasensitive osteosarcoma cell detection, pp. 503–509 (ref 71). Copyright 2016, with permission from Elsevier.). (E-a) UV–vis NIR spectra of AgNCs, AuNCs, and AuNCs/SiO₂ NPs. Experimental results for the extinction spectrum (green curve) and calculated results for the extinction (black curve), absorption (red curve), and scattering cross sections (blue curve) of AuNCs/SiO₂ NPs with an outer edge length of 29 nm, a wall thickness of 3.5 nm, and a SiO₂ shell thickness of 17 nm. (E-b) Typical TEM images (Reproduced from Wen, S.; Miao, X.; Fan, G. C.; Xu, T.; Jiang, L. P.; Wu, P.; Cai, C.; Zhu, J. *J. ACS Sens.* 2019, 4, 301–308 (ref 131). Copyright 2019 American Chemical Society.). (F-a) Schematics and typical TEM images of metallic Au@Ag core–shell rodlike nanomatryoshkas (RNMs) with 4-nitrobenzenethiol (NBT) embedded Raman reporters with different Ag shell thicknesses (scale bar: 50 nm). (F-b) Extinction spectra. EDS elemental mapping of (F-c) Au, (F-d) Ag, and (F-e) the overlay of Au and Ag and (F-f) the corresponding STEM image of a single NBT-RNM (Reproduced from Jin, X.; Khlebtsov, B. N.; Khanadeev, V. A.; Khlebtsov, N. G.; Ye, J. *ACS Appl. Mater. Interfaces* 2017, 9, 30387–30397 (ref 67). Copyright 2017 American Chemical Society.). (G) Characteristics of Ag/Ag-doped TiO₂ substrates: (G-a) UV–vis absorption spectra of as-synthesized pure TiO₂ and Ag/Ag-doped TiO₂ substrates prepared with different concentrations of AgNO₃ (0.1–0.7). (G-b) SEM image of Ag/Ag-doped TiO₂ substrates prepared with different concentrations of AgNO₃ (0.7 mM) (Reprinted with permission from Macmillan Publishers Ltd.: Zhou, L.; Zhou, J.; Lai, W.; Yang, X.; Meng, J.; Su, L.; Gu, C.; Jiang, T.; Pun, E. Y. B.; Shao, L.; Petti, L.; Sun, X. W.; Jia, Z.; Li, Q.; Han, J.; Mormile, P., *Nat. Commun.* 2020, 11, 1785 (ref 49). Copyright 2020, with permission from Springer Nature). (H-a) UV–vis absorption spectra of the SWCNT/C-DNA, SWCNT/AgNPs, and SWCNT/Ag/AuNPs nanoconjugates. (H-b) HADDF-STEM image of Ag and Au of the SWCNT/Ag/AuNPs nanoconjugate (Reproduced from Qin, X.; Si, Y.; Wang, D.; Wu, Z.; Li, J.; Yin, Y. *Anal. Chem.* 2019, 91, 4529–4536 (ref 59). Copyright 2019 American Chemical Society.). (I-a) UV-vis/NIR absorption spectra of SWNT-DNA (10 nm), SWNT-Au-PEG, and SWNT-Ag-PEG solutions (1 nm by SWNT content). (I-b) TEM images of the SWNT-Ag-PEG nanocomposite (scale bar: 50 nm) (Reproduced from Wang, X.; Wang, C.; Cheng, L.; Lee, S. T.; Liu, Z. *J. Am. Chem. Soc.* 2012, 134, 7414–7422 (ref 76). Copyright 2012 American Chemical Society.).

Since the NIR SERS substrates could create NIR-active hot spots with minimized fluorescence background and have a strong LSPR,²⁵ different shapes of the SERS substrates such as nanostars,²⁶ nanopyramids,²⁷ nanospheres,²⁸ nanorods,²⁹ and nanocages³⁰ have been explored in this region (Figure 2A–F). Also, there are many different types and sizes of anisotropic

nanoparticles, such as noble metal nanomaterials, semi-conductors, and carbon nanotubes, which show good SERS performance in the NIR (Figure 2G,I). According to the classical theory of EM, an important goal of SERS substrates is to achieve the maximum electromagnetic enhancement of single molecule sensitivity. On the basis of extensive studies of surface

enhancement signal amplification, the fabrication of substrates is controlled by continuous improvement to obtain optimized enhancement signals.

1.2.1.1. Noble Metal Substrates. Among the various types of substrates, noble metal substrates are the most widely used due to their excellent enhancement capability and easy synthesis in large quantities. Silver nanoparticles have stronger plasma resonance than gold in the visible region, but their advantages are lost in the near-infrared windows. Moreover, since the surface of silver nanoparticles is more susceptible to oxidation, it is toxic to mammalian cells, and silver nanoparticles have been used as antimicrobials.^{31,32} Thus, gold is the preferred substrate for biomedical applications in near-infrared regions. As early as 2008, Anker et al. introduced an LSPR sensor based on gold nanorods (AuNRs) with the characteristic LSPR of the NRs sensitive to the size and shape of the substrates.³³ However, the low penetration of the optical signals in the application of *in vivo* optical imaging leads to less acquisition of molecular information. To address these problems, Bhatia and co-workers have engineered gold nanorods (GNRs) as substrates to formulate a multifunctional platform based on SERS for multiplexed NIR detection.³⁴ The substrates were engineered to have the plasmonic resonance in the NIR region by modifying their size and shape. GNRs showed a plasmon resonance peak at 790 nm, which matched the NIR SERS excitation source (785 nm) and was crucial for SERS imaging *in vivo*. The probes were successfully used for efficient SERS imaging down to the attomole level. Before long, NIR active SERS nanopropes (NIR SERS dots) were developed.²⁵ When a galvanic replacement reaction was used, the plasmonic Au/Ag hollow shell (HS) assembled silica nanospheres (Au/Ag HSA) had a red-shift of their absorption bands from the visible (480 nm) to the NIR region (825 nm), which enabled them to induce more enhanced SERS signals at the NIR excitation light (785 nm). The study showed the NIR SERS nanopropes could generate strong SERS signals with high reproducibility, and the detectable signals could be acquired from animal tissues with a penetration depth up to 8 mm. Meanwhile, the existence of sharp edges and tips can provide high sensitivity changes of a local dielectric environment, leading to larger enhancements of the electric field around the nanoparticles, which are essential for the SERS analysis and LSPR.^{35,36} On the basis of the features caused by sharp edges and tips, an increasing number of synthetic procedures was developed by controlling the size/shape distribution. On the basis of that study, the same group further reported branched Au nanostars (AuNSs), which were synthesized by seeded growth.³⁷ Among them, the group found that two types of resonance modes were localized within the central part and the tips of such particles, respectively, which could be used for signal enhancement. However, during the long acquisition time required for SERS imaging, the nanoparticles may gather or degrade, leading to the separation of the reporter molecules from the substrates. To overcome these difficulties, Liz-Marzán and co-workers have fabricated multiplexing SERS nanopropes based on polyisobutylene-*alt*-maleic anhydride (PMA) coated AuNSs with LSPR modes in the first biological transparency window.³⁸ When the resonant Raman reporter IR-780 was encoded into gold nanostars with silica coatings and a protective PEG shell, the SERS intensity decreased by 3.2% and the hydrodynamic diameter increased by 0.4% at 37 °C for 72 h. Thus, reliable SERS signals over long time scales were observed. Compared with other reported SERS nanoparticles at the same period, the study demonstrated that the SERS signal intensity

was a ~400-fold improvement over that obtained by the LSPR in the NIR region and resonant Raman reporters. There is potential for the use of such SERS nanopropes in the detection of multiple biomolecules and cell types.

In recent years, hybrid SERS substrates using noble metal substrates incorporated with secondary functional materials have been given more and more attention.³⁹ Hybridization of metal substrate materials with carbon nanotubes, graphene, semiconductor materials, and other materials can produce synergies. Hybrid SERS platforms can integrate the inherent advantages of these materials and overcome the limitations of traditional novel metal substrates. For example, using the chemical coupling reaction to amplify Raman cross sections, these materials can strengthen the EM enhancement generated by the metal-only substrates. Besides, the analyte can be chemically captured by the surface linkers to locate it where the LSPR effect is at a maximum with high reproducibility. Consequently, the extensive future application of mixed SERS substrates will play an important role in the development of SERS probes.

1.2.1.2. Semiconductor Substrates. Lately, through the combination of a plasmonic metal and semiconductor, a series of photocatalytic self-cleaning SERS substrates were developed, which made the SERS substrates recyclable.^{40–42} In fact, the semiconductor itself has been proven to be the substrate material for SERS activity. Semiconductors have a frequency slightly lower than that of metal substrates. Although they have many more types of controllable properties including band gap, exciton Bohr radius, stable exciton production, control of stoichiometry, photoluminescence, low cost, and resistance to degradation, some have good SERS performances comparable to that of noble metal-based substrates.⁴³ In this section, we will focus on recent developments of semiconductor substrates in biological and biomedical applications in the NIR biological window since these substrates exhibit high stability, excellent reproducibility, and strong anti-interference ability.^{44–46}

It is known that the enhancement factor of semiconductors substrates can be ascribed to the photoinduced charge transfer (PICT) process between the substrate and the target molecules.^{43,47} In semiconductor molecular systems, the resulting strong vibrational coupling can result in a significantly improved molecular polarizability and an amplified Raman scattering cross section. For all resonance between reporter molecules and semiconductor substrates, the maximum SERS enhancement occurs at the edge of the semiconductor (valence or conduction) band, and these resonances are coupled and cannot be considered in isolation. To improve the PICT efficiency and further enhance the SERS signal, Lin et al. fully used both crystalline and amorphous structures and designed semiconductor-based black TiO₂ nanoparticles (B-TiO₂ NPs) with a crystal–amorphous core–shell structure.⁴⁸ In the substrate–molecule system of the crystal–amorphous core–shell structure, interfacial IPCT was facilitated by light-induced charge enrichment in the amorphous shell, and a PICT resonance was formed by the small band gap, high binding energy, and rich surface defect states of B-TiO₂. Significantly, under the irradiation of a 633 and 785 nm laser, B-TiO₂ NPs exhibited substantial SERS enhancement, which enabled the B-TiO₂ NPs to rapidly and accurately diagnosis MCF-7 drug-resistant breast cancer cells. A B-TiO₂ bioprobe with an 808 nm laser at 1.5 W/cm² was used for the photothermal treatment of drug-resistant MCF-7 cells to kill cancer cells. In addition, Han's group developed a Ag/Ag-doped TiO₂ nanostructure coated

with 4-mercaptobenzoic acid (4-MBA).⁴⁹ Under the irradiation of NIR light, when the laser irradiation time was extended, it was observed that the SERS signal of 4-MBA showed an exponentially cumulative increase and the Raman signal of the Ag/Ag-doped TiO₂ substrate exponentially and irreversibly decreased. The constructed SERS platform could provide an alternative technology strategy for future clinical applications, such as real-time monitoring ultrasensitive biological detection and catalytic reaction.

Additionally, semiconductor materials can be used as the substrates in SERS analysis and as good photothermal agents (PTAs), which can be used for the integrated treatment platform in SERS detection. In a study conducted by Guo and co-workers, the molybdenum oxide quantum dots (MoO₂ QDs) were synthesized as SERS substrates.⁵⁰ Since MoO₂ QDs with the Mo⁴⁺ state displayed a strong LSPR effect in the NIR region, they served as semiconductor substrates for ultrasensitive SERS analysis of aromatic molecules and antibiotics. Remarkably, MoO₂ quantum dots had strong near-infrared absorption with a photothermal conversion efficiency of 66.3%, which could be used as a PTA for cancer photothermal therapy. The SERS detection limit could reach 10⁻⁸ M, and their photothermal conversion efficiency enabled them to have potential for oncological diagnosis and treatment.

1.2.1.3. Carbon Nanotubes Substrates. In the past 30 years, CNTs have been one of the most novel nanomaterials due to their unprecedented high surface area, which allows the attachment of multiple cell-targeting agents.^{16,51,52} In the past 30 years, CNTs have been one of the most novel nanomaterials due to their unprecedented high surface area, which allows the attachment of multiple cell-targeting agents.

CNTs are mainly divided into single-walled carbon nanotubes (SWNTs) and multiwalled carbon nanotubes. In general, SWNTs have multiple Raman peaks, including free radical respiration patterns and tangential G-bands, which correspond to the vibrations of carbon atoms in the free radical and tangential directions, respectively.^{53,54} SWNTs have been used to measure the uptake dynamics of live cells and image multiple cell images with excitation in the NIR region.⁵⁵⁻⁵⁷

The enhanced SERS signals can be obtained by coating the surface of the nanotubes with noble metal nanoparticles. Liu's group coated noble metal on SWNTs for applications in SERS imaging and photothermal therapy under an NIR laser.⁵⁸ To advance the study of a similar substrate based on previous work, Qin et al. first synthesized a SERS probe composed of Ag/Au alloy nanoparticle-decorated SWNTs (SWNT/Ag/AuNPs) to visualize hypoxia.⁵⁹ The nanoconjugates had strong NIR plasmonic absorption and high Raman scattering enhancement capacity. Since SWNTs have a distinct Raman signal (2578 cm⁻¹), using azo alkynes (MPP) as SERS reporters modified on the nanoconjugate's surface, two Raman scattering signals of MPP (2207 cm⁻¹) and SWCNTs could be obtained under 785 nm excitation. In this work, under the hypoxia condition, MPP was gradually reduced by various reductases and cleaved off the surface of the SWNT/Ag/AuNPs. The characteristic Raman bands at 2207 cm⁻¹ from the alkynyl group of the MPP molecules were reduced or even disappeared, while the Raman signal at 2578 cm⁻¹ from the SWNTs remained unchanged, which could be used as an internal reference. Therefore, the hypoxia level could be detected and imaged according to the ratio of two peak strengths (I_{2578}/I_{2207}) positively correlated to the decrease in oxygen levels, which was confirmed in different types of cells and liver tissue after rat liver ischemia surgery.

1.2.2. Raman Reporter Molecules. Since SERS enhancement is very distance dependent, optical enhancement usually requires Raman reporter molecules to attach to or near the SERS substrate surface, even a few nanometers away. To achieve the desired distance between them, thiols and amines have been modified onto target molecules for its absorbance on the substrate surface. Nitrogen-containing or thiol fractions are often used due to their high affinity for gold and silver. Consequently, chalcogenide-containing and/or positively charged fluorophores are commonly used as Raman reporters that are attached onto the negatively charged substrate surface by covalent or electrostatic interaction, respectively.²⁸ Since noble metal nanoparticles can quench fluorescence, fluorescent dyes can be used as Raman reporters. When the analyte contains chromophore energy close to the excitation radiation, the use of such Raman reporters is conducive to the further enhancement of surface-enhanced resonance Raman scattering (SERRS), and the enhancement factor can be further enhanced by 100 times.⁶⁰

Moreover, the reporter molecules can generate a strong SERS signal with a large Raman scattering cross section. Different kinds of fluorescent dyes quenched by nanoparticles have been studied as reporter molecules, such as fluorescent dye indocyanine green (ICG),⁶¹ Cys,⁶² and aza-boron-dipyrromethene (BODIPY).⁶³ To precisely visualize the true extent of cancers, one kind of cyanine dye, IR-780, used as a SERRS reporter was developed.⁶⁴ Using a biocompatible encapsulation method, the resonant Raman reporter molecule could be effectively loaded onto the surface of the star-shaped gold core. When the advantages of LSPR were combined with resonance in the NIR window, the SERRS probes produced a high strength of SERS signals, about 400 times higher than other SERS nanoparticles that have been reported so far. The study suggested that SERRS nanostars represented a new class of molecular imaging agents, which were capable of mapping primary tumors, microscopic local tumor deposition as small as 100 μm, and precancerous lesions.

SERS signals can be improved by not only creating a larger Raman scattering cross section but also maximizing the loading of Raman reporters. When small aromatic mercaptan or aniline derivatives were used as Raman reporter molecules, reproducible SERS signatures could be generated due to the dense accumulation and uniform orientation of Raman reporter molecules on the substrate. In addition, with the maximum surface coverage ratio of the Raman reporters, the maximum SERS brightness could be generated by anchoring the Raman reporters on the bare surface of the substrates, which limited the loading amounts of the reporter molecules. The SERS probe with a gap structure has been developed rapidly because there are large numbers of hot spots inside it and the gap structure can increase the loading amount of reporter molecules.⁶⁵ Raman reporter molecules are often adsorbed on the AuNP surface as a sealer. The presence of reagents carrying thiols inhibiting the growth of anisotropic NPs makes the nanoparticle gap difficult to form. Li and co-workers proposed an effective strategy to increase the loading amount of the reporter molecules by using SERS probes directly added to the synthesis of the reporter molecules.⁶⁶ Using poly(*N*-(3-amidino)-aniline) (PNAAN) and Raman reporter molecules coadsorbed as capping agents on the AuNPs surfaces, AuNPs spontaneously self-assembled into spherical AuNPs by π - π stacking of PNAAN. Huge nanogaps were formed inside the AuNPs, resulting in 3D hot spots. Raman reporters were dispersed not only on the surface of the AuNPs but also within the AuNPs, and the 3D hot spots

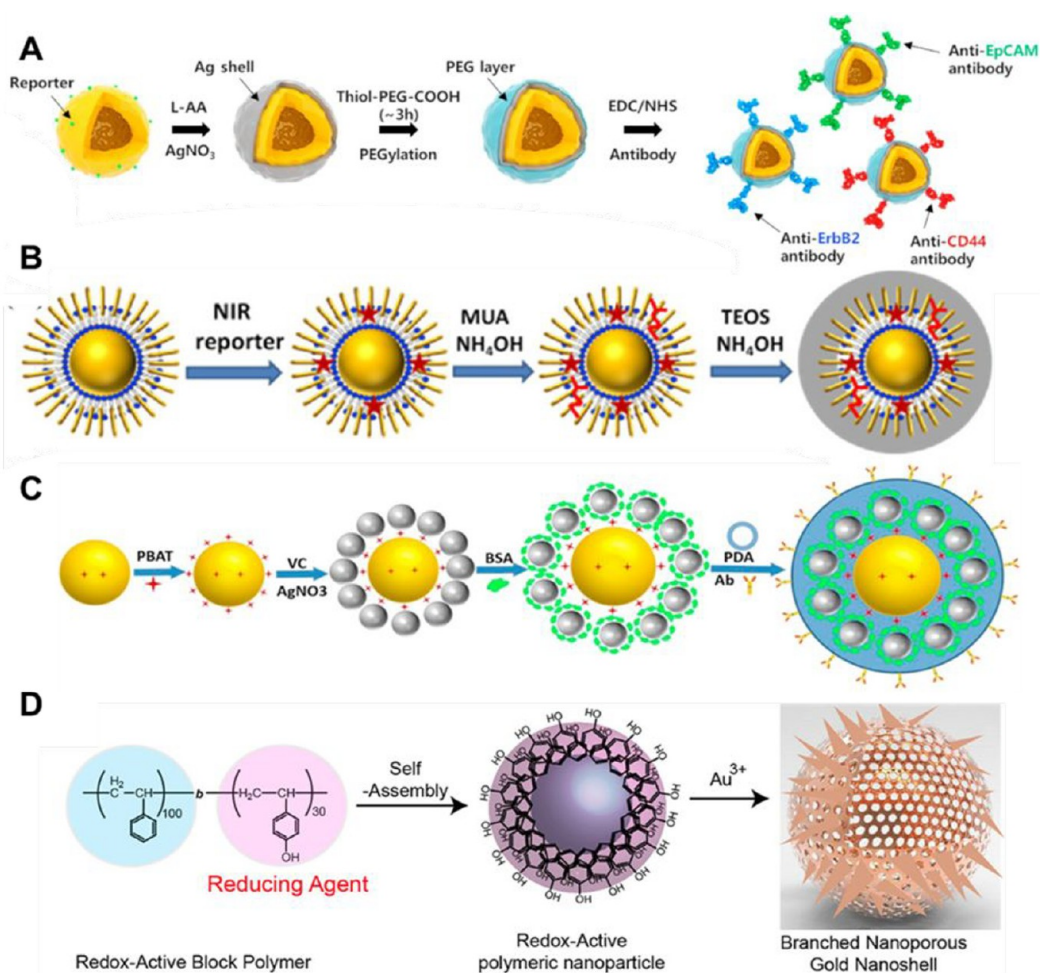


Figure 3. Typical types of encapsulations for SERS probes: (A) PEG coated Ag–Au hollow nanospheres (Reprinted from *Biosens. Bioelectron.*, Vol. 164, Choi, N.; Dang, H.; Das, A.; Sim, M. S.; Chung, I. Y.; Choo, J. SERS biosensors for ultrasensitive detection of multiple biomarkers expressed in cancer cells, p. 112326 (ref 68). Copyright 2020, with permission from Elsevier.). (B) Silica-coated waxberry-like NPs@SiO₂ SERS probes (Reproduced from Yin, Y.; Mei, R.; Wang, Y.; Zhao, X.; Yu, Q.; Liu, W.; Chen, L. *Anal. Chem.* 2020, 92, 14814–14821 (ref 69). Copyright 2020 American Chemical Society.). (C) Bovine serum albumin (BSA) and polydopamine (PDA) coated on the PBAT-Au@Ag (Reprinted from *Talanta*, Vol. 172, Chen, M.; Zhang, L.; Gao, M.; Zhang, X. High-sensitive bioorthogonal SERS tag for live cancer cell imaging by self-assembling core–satellites structure gold–silver nanocomposite, pp. 176–181 (ref 72). Copyright 2017, with permission from Elsevier.). (D) Self-assembly of redox-active amphiphilic diblock copolymers (Reproduced from Song, J.; Yang, X.; Yang, Z.; Lin, L.; Liu, Y.; Zhou, Z.; Shen, Z.; Yu, G.; Dai, Y.; Jacobson, O.; Munasinghe, J.; Yung, B.; Teng, G. J.; Chen, X. *ACS Nano* 2017, 11, 6102–6113 (ref 73). Copyright 2017 American Chemical Society.).

created by the formation of large nanogaps within the AuNPs were utilized to the maximum. 4-MBA was used as a Raman reporter because of its large Raman cross section and high affinity for AuNPs. SERS probes with 4-MBA were used as markers to modify the antibodies through the coupling reaction of carboxylic acid and amine. Using a 785 nm laser excitation source, the obtained SERS labels could be used for the immunoassay of staphylococcal enterotoxin B, and the significant improvements of their sensitivity were attributed to the high signal strength.

1.2.3. Capsulation. Optimal coatings are important for maintaining the photostability of SERS probes and minimizing the photothermal damage caused by laser irradiation, which may lead to degradation and photoreaction of the Raman reporters as well as unwanted molecules adsorbed onto the substrates.⁶⁷ The capsulation can be divided into a simple surface coating and biorecognition, which makes the probe possess biological stability and specific binding characteristics. Reporter molecules modified on the substrate could detach from traditional nanosubstrates *in vivo*.

Currently, the most widely used coating materials are PEG shell,⁶⁸ silica shell,^{69,70} bull serum shell,⁷¹ polydopamine (PDA),⁷² and amphiphilic diblock copolymer,⁷³ as shown in Figure 3. While coating material offers some advantages such as protection, it is unfavorable due to degradation and agglomeration problems. The typical SERS synthesis strategy usually uses dyes to be directly adsorbed on the substrate surface; subsequently, the surface coating is used to encapsulate dye molecules as well as to protect the stability of the probe to prevent nonspecific adsorption of other molecules. So far, the silicification of dye adsorbed nanoparticles has been the most effective in maintaining the stability and biocompatibility of SERS labels *in vivo*.⁷⁴ Since the silicification method depends on the high dye–metal affinity, it may be limited by adverse electrostatic interactions. The extension of the silicification process also generally leads to aggregation, size changes, uncontrolled dye incorporation, and surface charge manipulation. Notably, the silica coating increases the size of the metal core by approximately two times, which makes the synthesis of the smaller sized SERS probes hard. As an alternative to the silica

layer, Kircher and co-workers reported all-in-one nanoparticle coatings based on new NIR active poly(*N*-(2-hydroxypropyl) methacrylamides) (pHPMA).⁷⁵ Using hydrophilic NIR active polymer bonded to the substrate surface and NIR active conjugate cyanine dyes as a reporter after further modification, the surface coatings based on the hydrophilic polymers presented excellent biocompatibility and maximum colloidal stability over a long cycle time due to the stability of the robust amide conjugate between the dye and pHPMA as well as the stable covalent bond of the polymer to the surface of the gold nanoparticles. In their works, the extracted SERS signal indicated that the gold nanoparticles coated with a covalent gold–mercaptan bond polymer showed higher signal stability over 24 h. It was demonstrated that the SERS probes were excreted almost completely from the lymphatic vessels to the lymph nodes, which could be used to accurately detect lymph nodes.

To achieve further fast Raman imaging, a new coating by water-soluble SWNTs coated with noble metal nanoparticles was proposed by Liu and co-workers.⁷⁶ First, SWNTs were functionalized with negatively charged single-stranded DNA (ssDNA), and positively charged polypropylene amine hydrochloride (PAH) was attached onto the nanocomposites under an electrostatic force. Then, negatively charged gold seeds were deposited on the surface of DNA/PAH coated SWNTs (SWNT-DNA-PAH) to form SWNT-Au nanocomposites. Finally, the nanocomposites were further stabilized by a biocompatible polyethylene glycol coating. The nanotubes' SERS signals were enhanced because of the strong surface plasmonic resonance of the gold shell on the surface of the SWNTs. Both excitation and scattered light were selected in the NIR window, which was very suitable for optical imaging in biological systems. Also, the NIR absorption of plasmonic resonance could be used to enhance the photothermal ablation of the cancer cells. The resulting SWNT-Au-PEG nanocomposite was combined with the targeted ligand folate (FA) to achieve selective cancer cell labeling and rapid SERS imaging, and the excellent therapeutic effect demonstrated that SWNT-Au-PEG-FA designed an excellent photothermal agent for the ablation of cancer cells. With the shielding layer of the surface coating to improve stability, protection, and targeting molecules to the binding sites, reporters adsorbed on the Raman active substrate, strong and stable SERS fingerprint signatures were gained under the excitation light.

2. BIOSENSING AND BIOIMAGING IN THE NIR BIOLOGICAL WINDOW

Molecular biomarkers are dynamic indicators in the organism, and the abnormal fluctuation of various molecular biomarkers can be used as valuable hallmarks to monitor the existence and progression of various inflammations and diseases.^{77–79} Currently, the electrochemiluminescence immunoassay is the commonly used method to detect biomarkers in clinical cases. However, the extended data acquisition time and strict requirements of environmental factors still limit the improvement of clinical detection. Due to the wide emission spectrum and strong background autofluorescence, the commonly used fluorescence methods are often disturbed by color interference and are unable to carry out multiple types of detection. There is an urgent need to find a new multiplexing platform that can provide high sensitivity for the detection of multibiological molecules or pathogens.

Since NIR-responsive SERS analysis has less tissue spontaneous light interference, deeper imaging, less absorption, and lower scattering characteristics, they have aroused much attention in biological tissue.⁸⁰ The study of NIR active SERS probes *in vivo* started with instruments in the first NIR window by Nie and co-workers, which was successfully used for the targeting detection of *in vivo* tumor cells.⁸¹ More and more research groups have been employing SERS technology for *in vivo* applications that have focused on cancer cell imaging, detection, and therapy. The SERS study in the NIR window used a 785 nm diode laser mostly due to the high speed and detection sensitivity obtained by the dispersion Raman system of the silicon CCD detector with characteristics such as easy access and low cost. Additionally, NIR active SERS probes can provide useful information about an *in vivo* molecular structure with a narrow peak width, which makes multiplexing target detection in single excitation light possible.

2.1. Nucleic Acid. DNA is the primary biomaterial basis for storing, replicating, and transmitting genetic information. Current DNA testing methods, including sodium dodecyl sulfate polyacrylamide gel electrophoresis (SDS-PEG), polymerase chain reaction (PCR), and fluorescence, are mostly limited in their multiple detection capabilities. During these tests, the sample may also undergo changes and the loss of epigenetic information as well as carry a higher risk of contamination problems. The unique Raman spectra of molecules with significantly narrow bands make the technique suitable for multiple analyses. In addition, the technique can obtain a strong Raman signal from a low sample concentration and improve the sensitivity of its detection, additionally overcoming the potential contamination problem.

The DNA sequence is usually modified by thiol to facilitate attachment on the metal substrate surface. However, the covalently linked DNA sequence modified by thiol may undergo nonspecific adsorption, which will lead to different orientations on the substrate surface and even cause the changes in the obtained spectrum.⁸² Since the existing SERS probes can interact with DNA that may alter the native structure of the DNA and cause an inappropriate diagnosis, the modification of the molecules or substrates is required. Several strategies that were aimed at modifying substrate surfaces have been proposed, such as functionalizing the substrate surface with molecules, optimizing the electrostatic interactions between molecules by modifying the surface charge, or introducing a protective oxide layer. Due to the affinity between the nucleic acid molecule phosphate skeleton and the organic semiconductor substrate, the SERS substrate of the organic semiconductor has been widely used in DNA analysis.^{83–85} Using its natural inactive oxide layer as an important link between the molecule and the substrate, nonspecific adsorption on the metal surface was inhibited. Binding sites for various functional groups (e.g., carboxylic acid/phosphoric acid, silane, and amide) can be provided by using nanoscale surface oxide layers. In contrast to novel metals, nanoscale surface oxide layers can expand the types of molecules bound to their surfaces to promote molecule–substrate bonding. The presence of the oxide layer enables SERS to detect a wider range of nonresonant molecules, including biomolecules such as DNA in which unlabeled detection is very much needed. Tian et al. have designed Al nanocrystalline aggregates with broadband absorption characteristics displayed in the NIR region (850 nm), which could obtain the intensity of increased hot spots in the NIR window.⁸⁶ Through SERS spectrum recognition of ssDNA molecules with four different

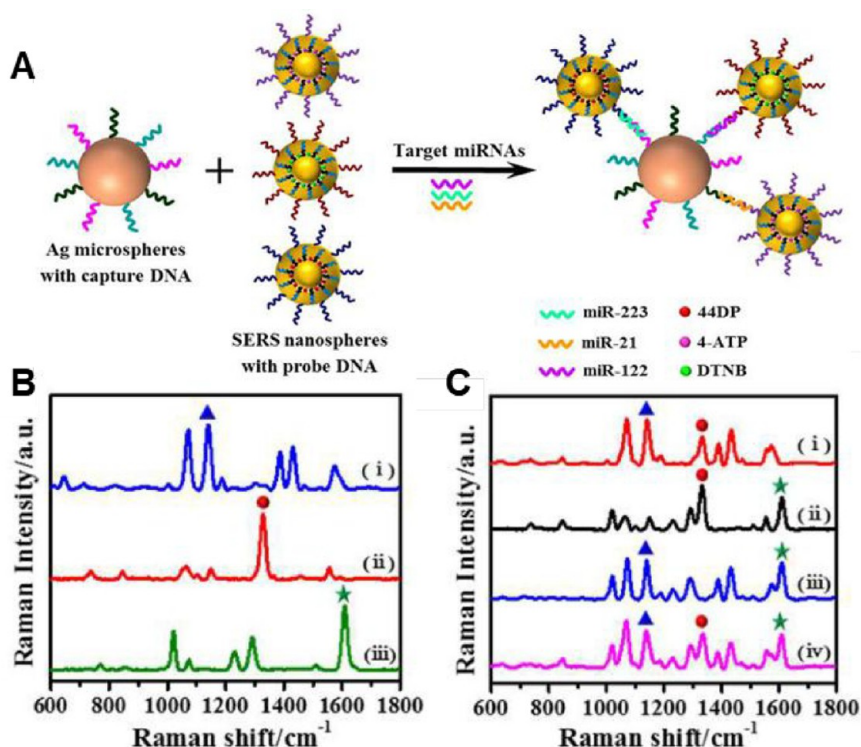


Figure 4. Strategies of NIR-active SERS analysis for biomolecules. (A) Schematic illustration of the multiplex SERS assay for triple-target miRNA detection. Three types of SERS nanoprobes were prepared via the functionalization of DNA detection on Au-RNNPs encoded by 44DP, 4-ATP, and DTNB. Each type of target miRNA was captured by the corresponding capture DNA anchored on Ag-HMSs, followed by hybridization with its own SERS nanoprobe, leading to the formation of coassembled multiple sandwich complexes. (B, C) SERS spectra of the nanoprobes obtained in the presence of single and multiple miRNAs. SERS spectra b-i, b-ii, and b-iii were obtained for the detection of target miR-21, miR-122, and miR-223, respectively. SERS spectra c-i, c-ii, c-iii, and c-iv were obtained for the multiplexed detection of a mixture of miR-21/miR-122, miR-122/miR-223, miR-21/miR-223, and miR-21/miR-122/miR-223, respectively (Reproduced from Zhou, W.; Tian, Y. F.; Yin, B. C.; Ye, B. C. *Anal. Chem.* 2017, 89, 6120–6128 (ref 93). Copyright 2017 American Chemical Society.).

bases, the quantitative unlabeled detection of single-stranded DNA was realized. In addition, in order to avoid nonspecific interactions between nucleic acid and probe systems and improve the detection sensitivity of organic semiconductors, Tan and colleagues have developed a new carbon-based organic semiconductor SERS probe, which could be reduced in size to the quantum level to show stable chemical properties in cell culture medium and remain inactive in the cell microenvironment.⁸⁷ Two different peaks were observed at 733 and 760 cm^{-1} (corresponding to adenine ring and cytopyrimidine ring respiration patterns, respectively, and the intensity changes and peak shifts of these two peaks could be attributed to structural changes caused by methylation). At the same time, the probe realized the detection of the molecular structure and gene expression aberrations of genomic DNA isolated from four cell models at femtomolar concentration under the excitation source of 785 nm. However, all of the above DNA tests are performed with DNA extracted *in vitro*, and 785 nm excitation light is the only kind of detector needed to avoid the loss of biological tissue.

However, it is very challenging to accurately determine the specific order of the bases in the DNA sequence from the SERS spectrum due to the variable combinations of the four bases in the DNA sequence. Since the use of DNA-labeled dye molecules could monitor the signal changes caused by the presence or absence of disease-related target sequences, NIR resonance of the dye produces SERRS with enhanced detection signals. The introduction of narrow bands also improved the potential for

multiple analysis.⁸⁶ With this in mind, an aptamer DNA was used to bind NIR responsive NP as the SERS probe to identify methicillin-resistant *Staphylococcus aureus* (MRSA).⁸⁸ Coupling NIR light with a NP in living systems has the benefit of producing thermal/photothermal effects and can be used for the dual killing of pathogens by binding natural antibacterial compounds (such as curcumin) to the probe surface.

However, since the traditional SERS signal reading relies on DNA probe and single-stranded target DNA hybridization, it is difficult to determine dsDNA and single-base mutation. Xiao and co-workers designed a SERS detection tool combined with lateral flow measurement (LFA) based on CRISPR-Cas12's unique trans-cutting effect and single base recognition of dsDNA or ssDNA (Figure 5A).⁸⁹ SERS tags modified by digoxin antibody in SERS lateral flow bars could be combined with biotin-DNA-digoxin to form SERS tag-DNA-biotin, and Cas12a/crRNA could be combined with streptavidin modified on the detection line (T line) The complex was inactive and could not cleave biotin-DNA-digoxin probes, while the trans-cleavage ability of Cas12a/crRNA to the DNA probes could be activated in the presence of target dsDNA. Therefore, the biotin-DNA-digoxin probe could be continuously cleaved to achieve the separation of digoxin and biotin, thus preventing streptavidin from connecting SERS tags on the T line. The reduction in the number of SERS tags on the T line resulted in the attenuation of SERS intensity and chroma. Since a single target DNA strand can trigger thousands of cleavages in the biotin-DNA-digoxin probes, the SERS signal attenuation could be amplified to

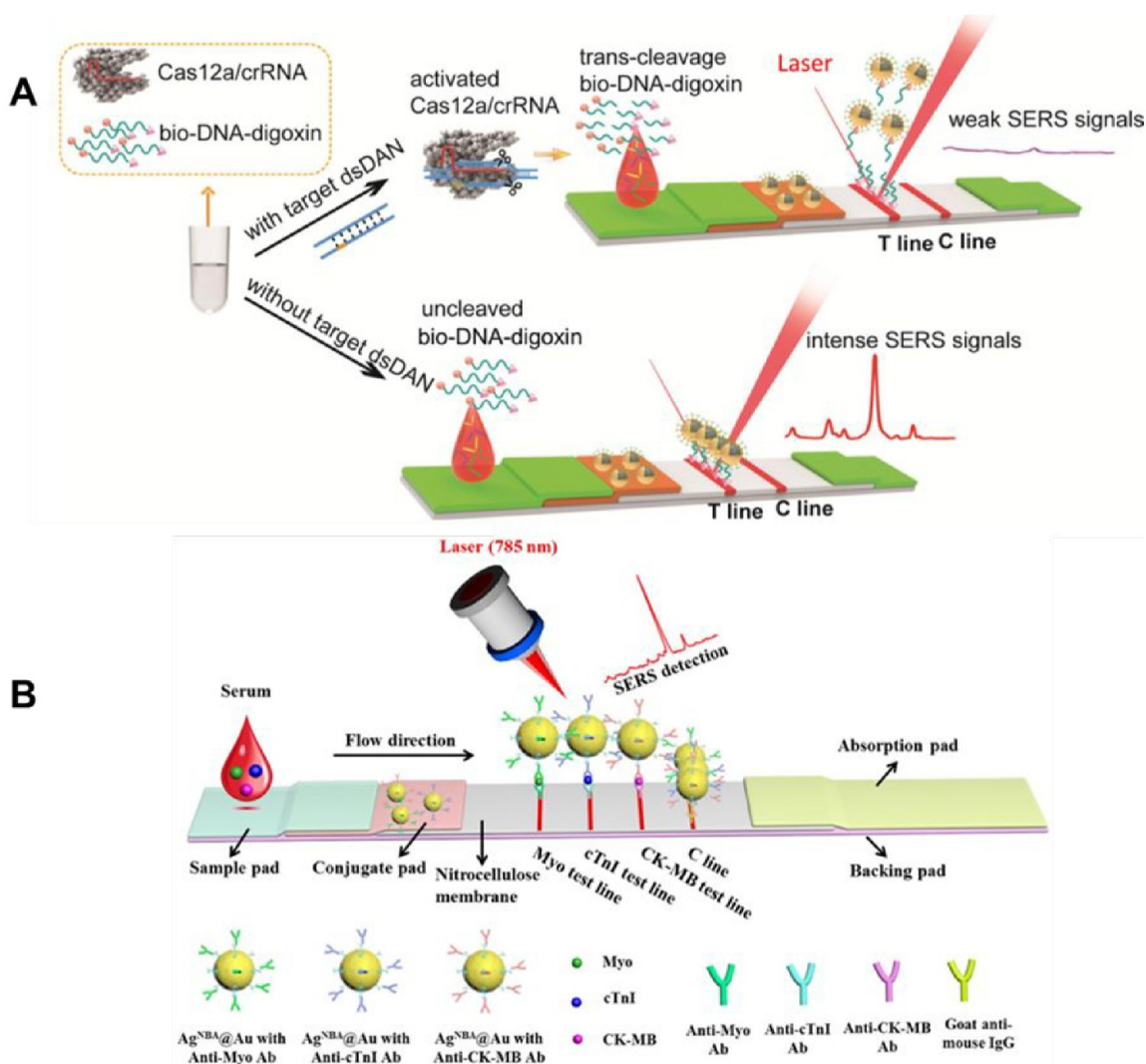


Figure 5. (A) Principle of the Cas12a-SERS strip for target dsDNA detection (Reprinted from *Chem. Eng. J.*, Vol. 429, Pang, Y.; Li, Q.; Wang, C.; Zhen, S.; Sun, Z.; Xiao, R. CRISPR-cas12a mediated SERS lateral flow assay for amplification-free detection of double-stranded DNA and single-base mutation, pp. 132109 (ref 89). Copyright 2022, with permission from Elsevier.). (B) Schematic illustration of the core-shell SERS nanotag-based multiplex LFA. The averaged Raman spectra of the three test lines for detection of Myo, cTnI, and CK-MB can be obtained (Reprinted from *Biosens. Bioelectron.*, Vol. 106, Zhang, D.; Huang, L.; Liu, B.; Ni, H.; Sun, L.; Su, E.; Chen, H.; Gu, Z.; Zhao, X. Quantitative and ultrasensitive detection of multiplex cardiac biomarkers in lateral flow assay with core-shell SERS nanotags, pp. 204–211 (ref 96). Copyright 2018, with permission from Elsevier.).

improve the detection sensitivity in the “off” model. The concentration of target dsDNA was positively correlated with the SERS intensity attenuation of the SERS strip T line. Combined with near-infrared region excitation light (785 nm) in biological systems, a LOD of 0.3 fM can be obtained in less than 1 h in simulated human serum samples when using HIV-1 dsDNA as a target model. On the basis of the target specificity of Cas12a, HIV-1 single-unit drug resistance mutations (M184V) of as low as 0.01% could be identified.

RNA exerts an enormous function on the translation process of proteins, among which microRNAs (miRNAs), a class of noncoding single-stranded RNA molecules with a length of about 22 nucleotides encoded by endogenous genes, have arisen interest. miRNAs participate in the regulatory activities of gene expression after gene transcription, most of which have high sequence conservation, expression timing, and tissue specificity. The dysregulated expression levels are related to pathological processes, especially human cancers, for conventional detection

methods through the traditional reverse transcription polymerase chain reaction (RT-PCR) and electrophoresis process, which are time-consuming and laborious^{90–92} Also, each target molecule converts only one signal to read. To detect multiple analytes simultaneously, Zhou et al. synthesized three types of DNA-conjugated SERS nanoprobe to detect three miRNA biomarkers (miRNA-21, miRNA-122, and miRNA-223), which were specific to hepatocellular carcinoma (HCC).⁹³ After irradiation with a 785 nm laser, each SERS probe exhibited its unique spectral fingerprint. Notably, the three target miRNAs were investigated simultaneously with a LOD down to 10^{-13} M (Figure 4).

2.2. Proteins and Small Biological Molecules. Small biological molecules are bifunctional groups composed of the basic organic matter of cells, which functions in main life activities like apoptosis and intercellular communication. Since various biological molecules can be considered biomarkers in physiological and pathological processes, the detection of small

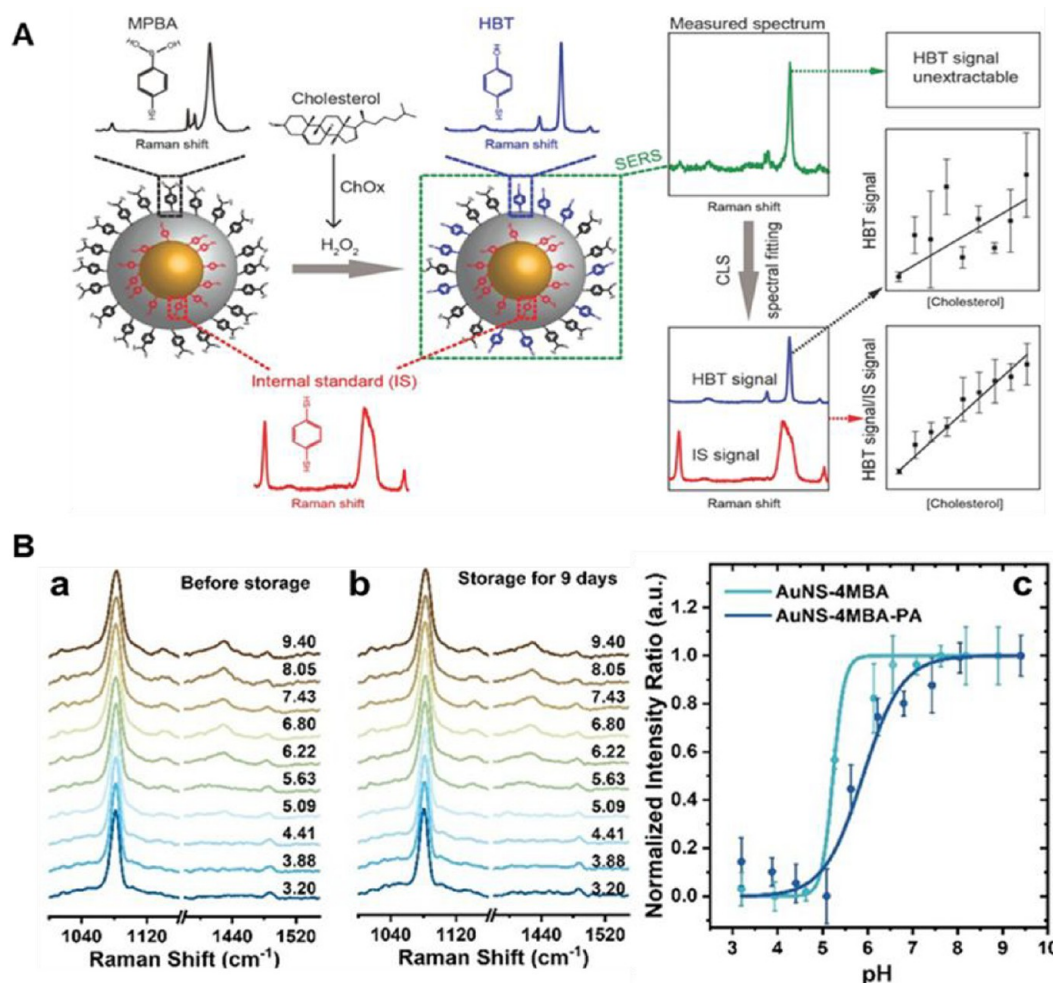


Figure 6. (A) Schematic illustration of SERS nanoprobe with the embedded internal standard for the quantitative detection of cholesterol via the Raman spectral fitting method (Reproduced from Surface-Enhanced Raman Nanoprobes with Embedded Standards for Quantitative Cholesterol Detection, Jiang, X.; Tan, Z.; Lin, L.; He, J.; He, C.; Thackray, B. D.; Zhang, Y.; Ye, J. *Small Methods*, Vol. 2, Issue 11 (ref 102). Copyright 2018, with permission from Wiley.). (B) Normalized SERS spectra of AuNS-4MBA-PA in complete cell culture media with different pH values before (a) and after (b) storage for 9 days. (B-c) Normalized pH response curves using pH probes with and without polyarginine (AuNS-4MBA-PA and AuNS-4MBA) (Reproduced from Zhang, Y.; Jimenez de Aberasturi, D.; Henriksen-Lacey, M.; Langer, J.; Liz-Marzán, L. M. *ACS Sens.* 2020, 5, 3194–3206 (ref 110). Copyright 2020 American Chemical Society.).

molecules is essential and effective in clinical application. For example, biomarkers such as myoglobin (Myo), myocardial troponin I (cTnI), and creatine kinase-MB (CK-MB) play vital roles in the initial phase diagnosis of acute myocardial infarction (AMI). Currently, enzyme linked immunosorbent assay (ELISA), fluorescence, electrochemistry, and immunosuppression are the most widely used methods.^{94,95} However, current detection methods have limited range and are time-consuming, often leading to untimely treatment and even death of AMI patients. To solve this problem, a multiple lateral flow assay (LFA) (SERS LFA) was constructed to simultaneously, fast, and quantitatively detect three different myocardial markers at low cost and with a miniaturized 785 nm laser (Figure 5B).⁹⁶ In this study, the 785 nm laser showed the advantage of being suitable for the development of integrated and mini-type point of care testing (POCT) instruments for LFA analysis. To further study the immune targeting ability of antibodies for the diagnosis of many diseases, many antibody markers were validated by studies that were utilized to select antibodies with high specificity and desired functions for effective antibody-based therapies. For example, Lee and co-workers established a validation process, a

NIR-SERS-based strategy to validate antitetraspanin-8 antibody candidates for human colon cancer, *in vivo* after *in vitro* antibody screening.⁹⁷ The technique of SERS provides potential approaches for developing multifunctional detections systems in real applications.

Cholesterol, a major component of the cell membrane, is another important small molecule. Also, the cholesterol in human serum is the essential synthetic precursor for oxidized sterols and sterol hormones, such as bile acid, steroid hormones, and vitamin D. An excessive cholesterol level is often associated with cardiovascular diseases including coronary heart disease, atherosclerosis, and so on. Many technologies have been used for the detection of cholesterol levels. Fluorescence imaging based on cholesterol-binding proteins has been applied in the *in situ* quantification of cholesterol.^{98,99} However, the fluorophore may interfere with the normal functions of the labeled components.¹⁰⁰ Nondestructive and real-time detection, which could avoid some interference toward cell function, can be provided by SERS methods. Ren and co-workers developed a new SERS sensor with an internal reference to detect the changes of small molecules in the metabolic process of the body

in real time¹⁰¹ through combining the Au–Ag core–shell NPs with an internal standard calibration molecule; it exhibited quantitative detection of H₂O₂ and cholesterol inside fixed live cells. To deal with the limitation of the low reproducibility of the SERS signal, Ye et al. first fabricated the Au–Ag core–shell embedded with 1,4-benzenedithiol molecules as a Raman internal standard, since embedding internal standards could avoid additional NP aggregation-induced electromagnetic hot spots or the uniformity of the hot spots and disturbance from the biological environment to correct the fluctuation of samples and measuring conditions (Figure 6A).¹⁰² Then, target reporter molecule 4-mercaptophenylboronic acid (4-MPBA) was adsorbed onto the shell as the complete SERS nanoprobe. With the reaction between 4-MPBA and H₂O₂ that converts 4-MPBA into 4-hydroxybenzenethiol (4-HBT), the change of SERS signal was obtained and could be used to quantify the amount of H₂O₂. Similarly, H₂O₂ yielded from the reactions between cholesterol and ChOx could be used to quantify the consumption of cholesterol. Due to the excellent penetration depth of near-infrared wavelengths in biomedical applications, a 785 nm NIR laser was chosen to excite the Raman spectrum of molecules anchored on it. The signal intensity from the complexed SERS spectra was obtained with good reproducibility and greater detection sensitivity.

2.3. Dynamic SERS Sensing of Biological Environment.

In a variety of pathological and physiological processes, the body will undergo oxidative stress and cause cell damage. During this process, there are many reactive oxygen species and reactive nitrogen species produced, such as peroxynitrite (ONOO⁻), HClO, and NO, which can be used as important indicators for early diagnosis of the body's dysfunction process and evaluation of drug efficacy.^{103–105} Li and co-workers developed a novel SERS nanoprobe using 3-thiapphenyl borate (3-MPBAP) as the Raman reporter attached on the AuNP surface to image ONOO⁻ produced by macrophages under oxidative stress.¹⁰⁶ With the increase of ONOO⁻ concentration, the borate portion of 3-MPBAP was converted to hydroxyl. The SERS peak at 882 cm⁻¹ showed an increased response, which significantly changed the SERS spectrum of the nanoprobe. Since the intensity of the peak at 993 cm⁻¹ was almost unchanged before and after the addition, the peak at 993 cm⁻¹ was selected as the internal control. Using I_{882}/I_{993} as the ratio peak and 785 nm as the excitation laser, the SERS spectrum of the nanoprobe had a good correlation with the concentration of ONOO⁻. To improve the efficiency of detection, the same group developed a dual-reaction nanosensor using 3,4-diaminophenylboronic acid pinacol ester (DAPBAP) modified onto AuNPs to simultaneously monitor the changes of NO and ONOO⁻ concentrations in the oxidative stress process of macrophages Raw264.7.¹⁰⁷ In the presence of ONOO⁻, the borate phenyl ester group of DAPBAP was transformed into the phenolic group, and the SERS peaks at 538 cm⁻¹ appeared, which was consistent with the increase of ONOO⁻. When the NO molecule was introduced, the *o*-phenylenediamine moieties of DAPBAP were converted into the triazole moieties, and the peak appeared at 786 cm⁻¹, which was consistent with the NO increase. There was no change before and after the addition at the peak of 584 cm⁻¹, which was selected as an internal control. In the study, I_{538}/I_{584} and I_{786}/I_{584} were linearly related to the ONOO⁻ and NO concentrations, respectively. The results showed good satisfaction for the simultaneous detection of NO and ONOO⁻ in live cells with an excitation laser at 785 nm.

Due to the continuous interchange of material between the intracellular and extracellular microenvironment, the metabolic activities of cells and the constant changes in the extracellular environment will inevitably affect many biological processes, including apoptosis, endocytic processes, signal transduction, enzymatic activity, etc. The accurate detection of intracellular pH (i-pH) pushes forward immense influences on understanding cellular processes. Many approaches for imaging i-pH in living cells, such as potentiometric pH sensors and fluorescent pH sensors, have been reported.^{108,109} However, long-term dynamic imaging acquisition and fixed dyes inevitably negatively affected cell function. This imaging method was limited to two-dimensional images without considering the volume changes during the detection process, losing the ability to obtain dynamic i-pH information on live cells. In order to intuitively reflect the changes in the dynamic distribution of pH within a single cell, Liz-Marzán and co-workers have reported a pH-responsive plasmonic nanosensor to obtain three-dimensional SERS imaging of the comprehensive i-pH spectrum in living cells (Figure 6B).¹¹⁰ With AuNSs as substrates functionalized by 4-MBA and coated with a cationic polymer poly-L-arginine hydrochloride (PA) as a protective coating, the pH-responsive probe "AuNS-4MBA-PA" was developed. The probe was sensitive to the NIR excitation laser, thus avoiding cell autofluorescence and reducing phototoxicity. On the one hand, since PA was an arginine-rich polypeptide with a high positive charge, it bound to the cell membrane and transferred to the cytoplasm through electrostatic interaction, which contributed to the endocytosis of the probe and its transport in the cell. On the other hand, the permeability of the PA layer facilitated the diffusion of ions from the external medium, thus allowing the protonation state to change at different local pH values. Therefore, this probe exhibited high cell internalization efficiency and colloidal stability. Using a 785 nm laser as the excitation source, 3D SERS imaging of i-pH was performed on a confocal Raman microscope.

Additionally, the accurate detection of extracellular pH is important for acidification of the extracellular microenvironment. It is related to the metabolism of tumor cells through switching from oxidative phosphorylation to aerobic glycolysis (Warburg effect) in cancer cells.¹¹¹ Li and co-workers reported a pH responsive ratiometrically SERS probe embedded NIR dye IR7p, and the measured physiological pH with high sensitivity and tissue penetration depth though spatial orientation induced intramolecular energy transfer (SOIET) with pH-responsive absorbance under the NIR excitation laser.¹¹²

2.4. Pathogens Identification. Chronic infections are common in wound healing, and the best way to treat infectious diseases is to detect them as soon as possible so that they can be treated once diagnosed. Due to similar early acute infectious disease symptoms, diagnosis based on clinical symptoms alone is difficult.

Highly accurate diagnostic tests are essential to ensure effective and efficient pathogen identification. For example, early Ebola virus (EBOV), a severe infectious virus that erupted in West Africa, diagnosis played a crucial role in infected patients, and RT-PCR was the primary detection method. Even though RT-PCR could provide an accurate diagnostic, appropriate temperature requirements for the detection reagent and complex operation process limited its clinical use. Weidemaier and co-workers developed a SERS-based multiplexed diagnostic platform with immunoassays through a pair of capture/detection antibodies similar to the immunomagnetic bead

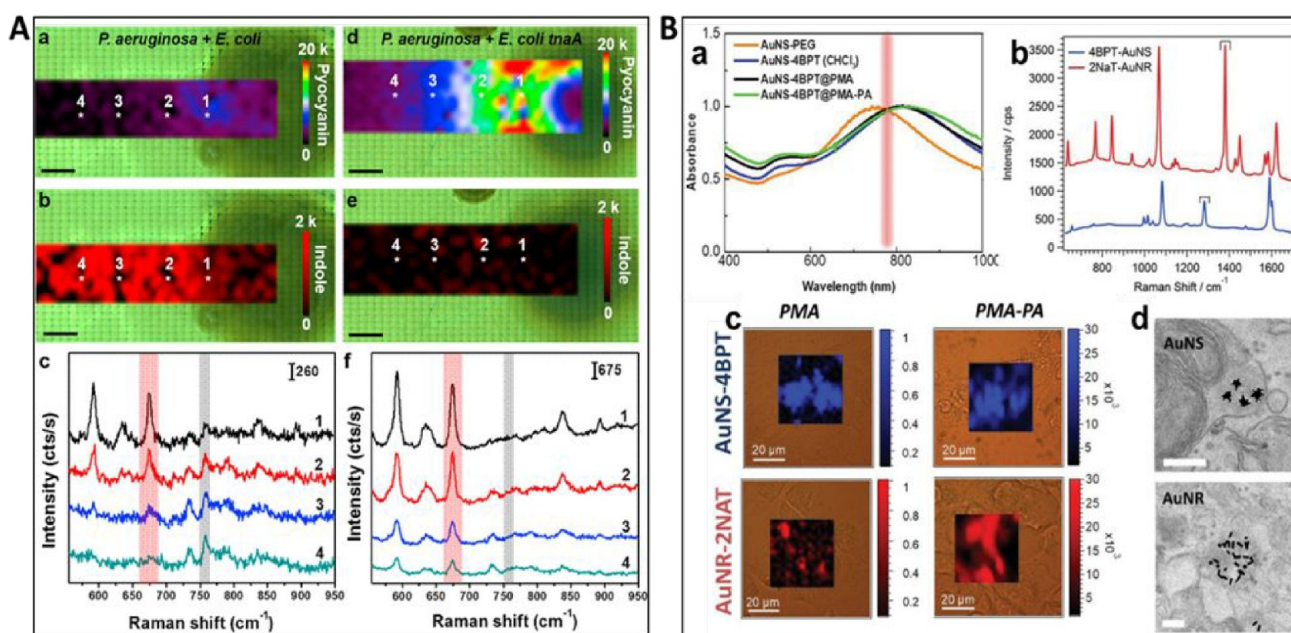


Figure 7. (A) SERS mapping of pyocyanin at 675 cm^{-1} (a) and indole at 760 cm^{-1} (b) produced by a colony of *P. aeruginosa* and *E. coli*. (A-c) Representative SERS spectra recorded at the points indicated with the white asterisks in (a) and (b). (A) SERS mappings of pyocyanin at 675 cm^{-1} (d) and indole at 760 cm^{-1} (e) produced by a colony of *P. aeruginosa* and *E. coli tnaA*. (A-f) Representative SERS spectra recorded at the points indicated with the white asterisks in (d) and (e). The red and gray shaded bars indicate pyocyanin (675 cm^{-1}) and indole (760 cm^{-1}) specific peaks. The spectra were acquired with a 785 nm laser line, $20\times$ objective, and a laser power of 4 mW . Scale bars are 1 mm (For the interpretation of the references for the colors in this figure legend, the reader is referred to the web version of the article.) (Reprinted from *Appl. Mater. Today*, Vol. 14, De Marchi, S.; Bodelón, G.; Vázquez-Iglesias, L.; Liz-Marzán, L. M.; Pérez-Juste, J.; Pastoriza-Santos, I. Surface-enhanced Raman scattering (SERS) imaging of bioactive metabolites in mixed bacterial populations, pp. 207–215 (ref 119). Copyright 2019, with permission from Elsevier.). (B-a) Spectra prior to encoding, after coating with the respective Raman-active molecules (AuNR-2NAT and AuNS-4BPT), after PMA encapsulation (AuNP-RaR@PMA), and further coated with PA (AuNP-RaR@PMA-PA). (B-b) Raman spectra of AuNR-2NAT and AuNS-4BPT encoded NPs. (B-c) Cell viability and NP uptake in HDF cells. Brightfield optical images overlaid with colored SERS maps of HDF containing AuNS-BPT (blue) and AuNR-2NAT (red) NPs, expressing either anionic (left) or cationic (right) surface charges. Scale bars: $20\text{ }\mu\text{m}$. (B-d) TEM images of AuNS-4BPT@PMA-PA and AuNR-2NAT@PMA-PA NPs in HDF cells. Scale bars: $200\text{ }\mu\text{m}$ (Reproduced from Using SERS Tags to Image the Three-Dimensional Structure of Complex Cell Models, Jimenez de Aberasturi, D.; Henriksen-Lacey, M.; Litti, L.; Langer, J.; Liz-Marzán, L. M. *Adv. Funct. Mater.* Vol. 30, Issue 14 (ref 120). Copyright 2020, with permission from Wiley.).

method, which could be used to differentiate Ebola from endemic febrile diseases in austere environments.¹¹³ Since clinical samples (blood) have minimal absorbance in the NIR, which could enable the SERS signal to be detected directly in whole blood, the NIR was chosen as the excitation laser. Because of the high laser power level of visible light, the structure of pathogenic bacteria may change and even destroy the detection of pathogenic bacteria. Therefore, under the excitation of light laser, the repeatability and stability of pathogen detection in SERS were poor, which limited its practical application in biological sample detection. To solve this problem, a low-power NIR laser was adopted. Zhang and co-workers used a NIR active SERS probe to detect *E. coli*.¹¹⁴ However, the manipulation of the shape and size of the metal substrate to redshift its LSPR into the NIR region requires a very complex synthesis process. This team integrated the microfluidic chip and SERS under an NIR laser for the first time to solve the problem of low detection sensitivity. With the deep penetration depth of the 785 nm laser, the film damage was relatively small. Also, the microfluidic chip provided a good living environment for bacteria. In the process of the bacterial test, the reproducibility of the SERS test state and the stability of the probe structure were realized.

Immunomagnetic bead-assisted SERS immunosensors have been continuously improved in later studies. Polymer nanoparticles can be used as a nanostructure substrate as well as a magnetic chelator of the target substance with a double function.

Thus, a probe using the functionalized polymer magnetic nanoparticles (FPMNPs) with a surface dione functional group was designed by Singh and co-workers.¹¹⁵ The surface dione functional groups were covalently coupled to antibody as capture probes that promoted the capture of bacteria with 5,5'-dithiobis (succinimidyl-2-nitrobenzoate) as Raman labels. The results showed that the LOD of 10 cells per mL of *S. typhimurium* was obtained by SERS detection.

2.5. NIR SERS Bioimaging. Although the molecular fingerprints obtained by Raman are unique, the intrinsic signal of Raman itself is weak, but in the presence of the substrate, a strong SERS signal will be generated under the irradiation of the incident laser, which can be detected by the detector. With the continuous development of SERS technology, the strong SERS signal at the hot spot of the substrate has been widely used for SERS imaging of different molecules and cells. In the past decades, SERS imaging has aroused a wide interest in imaging active molecules, living cells, and bacteria.^{116,117}

Molecular imaging is an important analysis for visualizing and measuring physiological and pathological processes in living systems. In order to further delve into the potential of SERS imaging, Liz-Marzán's team designed a nanocomposite material with excitation light located in the biological transparent window (785 nm).¹¹⁸ When the reporters were combined with different SERS substrates embedded in the biodegradable poly(lactic acid-total-glycolic acid) nanomaterial, the distribu-

tion of the composite probe was imaged and monitored by Raman microscopy, and its biocompatibility and long-term stability were verified, which laid a foundation for the trajectory tracking and biotransformation function of nanoparticles in human tissues. Soon, the same group developed a glass slide platform on the basis of a gold substrate that had a wide range of plasma coupling. The detection and imaging capabilities of the platform were used to explore the interaction between the two bacterial growth processes, and the interaction between different bacterial communities by *in situ* imaging of cellular metabolites such as indole and pyocyanin has been successfully visualized and tracked in real time.¹¹⁹ Under the excitation light of 785 nm, SERS mapping was carried out on the specific SERS peaks of pyocyanin at 675 cm^{-1} and indole at 760 cm^{-1} (Figure 7A), so as to discuss the promoting and/or inhibiting effects of the *Pseudomonas aeruginosa* and *Escherichia coli* coculture.

In addition, the biodegradable composite probe was also expected to be used for drug delivery as an alternative therapy. The team went on to complete the latter work. Since the 3D imaging model can better represent the metabolic details *in vivo* and *in situ*, SERS imaging research on the biological samples in the 3D model was carried out (Figure 7B).¹²⁰ Through the use of AuNS- and AuNR-based NIR active SERS probes, the endocytosis and biological compatibility of the nanoparticles in the fibroblasts were successfully observed. The results showed that the nanoparticles could be retained in the cells through endocytosis, and the normal division of cells would not be affected. Additionally, Gravely and Roxbury designed a noncovalent hybridized probe platform with a DNA-modified SWNT.¹²¹ Biocompatibility and surface functionalization were achieved with the DNA-modified surface. The probe successfully accumulated and aggregated in the lysosomal vesicles through endocytosis, which was imaged by the inherent NIR fluorescence and G-Raman peak dual-mode spectrum of the SWNT. According to the high sensitivity of the Raman probe itself, it could respond to changes in the intracellular environment (pH, temperature, etc.). The nanomaterial successfully realized the dynamic depiction of the endocytosis event of a single cell.

3. THERAPY BASED ON NIR SERS PROBES

NIR active SERS probes have higher penetration depth and lower scattering and autofluorescence background than visible light. In particular, when aiming at the resonance in the longer wavelength of the NIR window, it is worth noting that the nanoparticles would become better absorbers than the scatterers, which promotes the probes to generate controlled heating in response to laser irradiation. Therefore, SERS probes in this region were mainly used to ablate tumor cells by heating and can assist the self-assembly and disassembly of nanoparticles under the influence of temperature/pH to obtain drug release.^{73,122–124}

On the basis of the multifunctional characteristics of SERS probes, SERS image-guided therapeutics nanoplatfoms and multimodal methods combined with other imaging technologies have attracted widespread attention. The multifunctional theranostic nanoplatfom is a collaborative system with optimal treatment and diagnosis capabilities, which can be used for early cancer diagnosis, accurate cancer prognosis, and assessment of cancer treatment by incorporating cancer specificity, imaging, and treatment methods into nanomaterials. Simultaneously, the nanoplatfom can simulate the treatment and diagnosis system to deliver small molecules, peptides, and proteins and perform

real-time and *in situ* monitoring, imaging, and therapy functions for disease diagnosis, thereby significantly improving the treatment efficiency. In this section, we review the developments in multimodal image-guided and multifunctional treatment platforms in the past decade. It is important to integrate imaging and treatment into a one-in-all platform for high-performance therapeutics, which is also a major challenge and opportunity in cancer research.

3.1. Photothermal Therapy. **3.1.1. Photothermal Tumor Cell Eradication.** Early diagnosis and effective therapy are important for cancer patients. Since precise cancer cell mapping and effective treatment are crucial to prolonging cancer patients' lives, a new SERS analysis platform with nondestructive real-time detection features stands out. Photothermal therapy (PTT) is a remote-controlled therapeutic method that converts NIR light energy into locoregional hyperthermia, including irreparable cellular damage and tumor eradication. Utilizing large absorption cross sections of nanomaterials, NIR light-mediated phototherapy based on the SERS nanoprobe has raised attention for improving *in vivo* treatment.¹²⁵ It is well-known that the intrinsic hot spots generated by the anisotropic metal nanoparticles are beneficial to the electromagnetic amplification of the excited SERS signal and can have higher photothermal conversion efficiency.

The gold nanostars (AuNSs) with tree-branch tips were selectively etched on the gold nanoparticles by electron replacement.^{126,127} AuNSs contain multiple sharp peaks, which can significantly enhance the local electromagnetic field due to the tip-enhanced plasmonic effect.³⁵ Compared with other gold nanoparticle shapes, the design of the AuNSs can result in the enhancement of the SERS signals, excellent photothermal conversion efficiency, and a highly concentrated heating effect.¹²⁸ They were designed and integrated to have multiple functionalities with a greatly enhanced LSPR effect under NIR illumination. To ensure tumor-specific accumulation with minimal retention in other normal organs and maximize photothermal conversion efficiency, the new AuNSs were synthesized for tumor-targeted SERS imaging and NIR-I/II light-triggered photothermal therapy.¹²⁹ Arginine–glycine–aspartic acid (RGD) had high affinity with the $\alpha v\beta 3$ integrin, which was overexpressed in A549 cells. 4-MBA and RGD were labeled onto metal substrates, and the AuNSs were further designed to be multifunctional SERS probes. In the process, the A549 human lung adenocarcinoma cell membrane receptor was selectively targeted by RGD molecules, and then, the nanoprobe was introduced into the cell through RGD-mediated endocytosis. Because the multifunctional AuNSs had a broad NIR absorption band, the probe could be used as a bright SERS probe. In order to avoid fluorescence interference of biological tissues and realize photothermal treatment of deep tissue tumors, the designed NIR SERS probe had good photothermal effects in the NIR-I and NIR-II windows, and tumor cells were fully killed with the working power below the skin-tolerance threshold.

Additionally, Au nanocages (AuNCs) also are representative of typical plasmonic nanostructures. Because of their internal hollow and wall porous structures with a large free volume, individual AuNCs have superior internal and external surface coupled electromagnetic fields as well as accommodate more Raman molecules.¹³⁰ Zhu and co-workers have engineered an aptamer-conjugated AuNCs/SiO₂ core–shell bifunctional SERS probe.¹³¹ Using AuNCs as substrates, 4-MBA worked as a bright Raman reporter with a large cross section and excellent

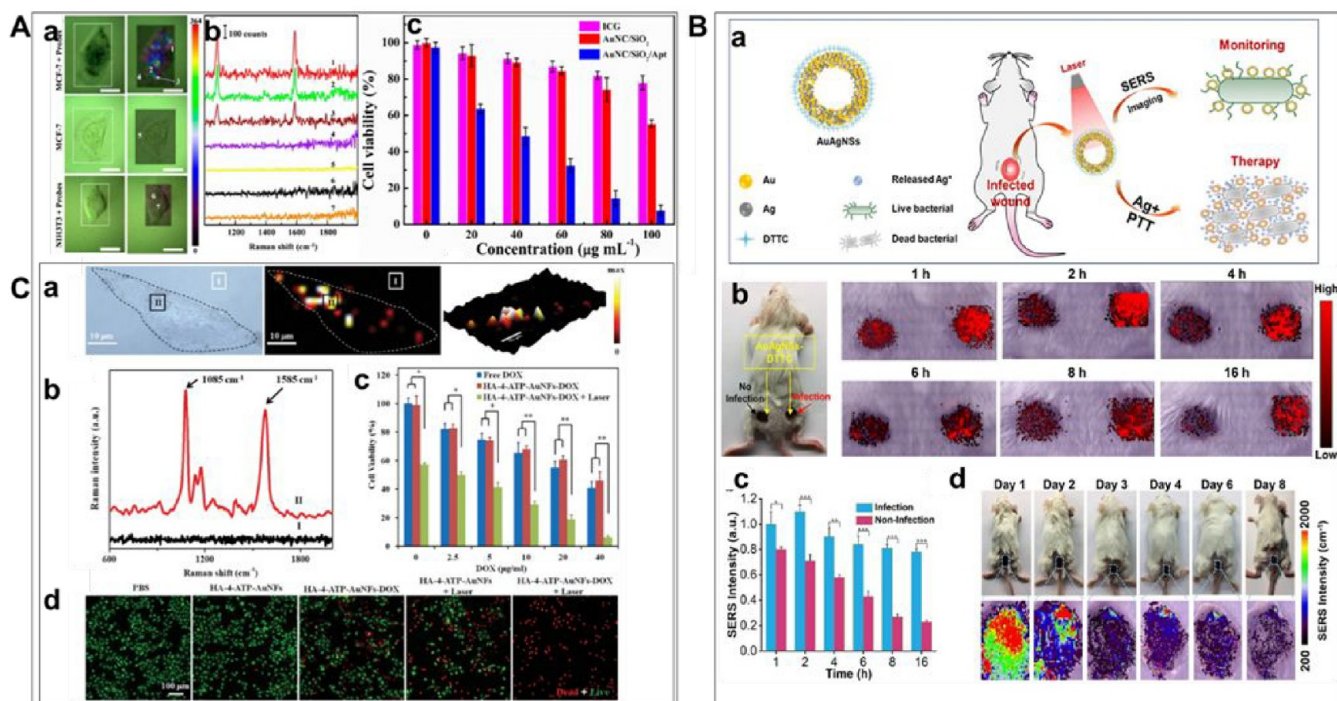


Figure 8. Therapy based on NIR responsive SERS probes. (A-a) SERS images of single MCF-7 (or NIH3T3) cells with and without AuNCs/SiO₂/Apt nanoprobe (left: bright field; right: SERS mapping images based on the intensity of 1588 cm⁻¹). (A-b) Representative Raman spectra at different spots indicated in (A-a). Dotted rectangles represent SERS imaging areas. Scale bars: 20 μm. (A-c) Viability of MCF-7 cells cultured with ICG, AuNCs/SiO₂ NPs, and AuNCs/SiO₂/Apt nanoprobe at different concentrations with laser irradiation (1.5 W/cm²) for 5 min, respectively. Note that the concentrations of AuNCs/SiO₂ NPs and AuNCs/SiO₂/Apt nanoprobe have been normalized in all photothermal experiments. Five sample replicates were conducted in all experiments. In addition, 20, 40, 60, 80, 100, and 120 g mL⁻¹ of the AuNCs/SiO₂/Apt suspension corresponded to the CP of 9.78×10^9 , 1.96×10^{10} , 2.93×10^{10} , 3.91×10^{10} , 4.89×10^{10} , and 5.87×10^{10} particles per mL, respectively (Reproduced from Wen, S.; Miao, X.; Fan, G. C.; Xu, T.; Jiang, L. P.; Wu, P.; Cai, C.; Zhu, J. J. *ACS Sens.* **2019**, *4*, 301–308 (ref 131). Copyright 2019 American Chemical Society.). (B-a) Illustration of the therapy scheme for a multifunctional gold–silver nanoshell (AuAgNS) nanosystem. When irradiated with a near-infrared laser, not only are the Gram-negative *Escherichia coli* and Gram-positive *S. aureus* bacterial strains eliminated, but also the colony expansion of bacteria through the synergistic effect of photothermal therapy and the release of silver ions is inhibited. (B-b) Photographic image of a Balb/c mouse with noninfected and infected wounds after applying AuAgNSs-DTTC and SERS images of noninfected (left) and infected (right) wounds at different time points after AuAgNSs-DTTC application. (B-c) Quantification of SERS intensity of noninfected and infected wounds after applying AuAgNSs-DTTC. Data are presented as the mean and standard error of the mean (SEM). Three replicates were performed for each experiment. (B-d) Photographic images and corresponding pseudocolor-coded SERS images of AuAgNSs-DTTC-applied wounds for up to 8 days after treatment. All measurements were performed with an excitation laser wavelength of 785 nm at 3 mW for 0.1 s at the concentration of 18.7 μg mL⁻¹ (*: $p < 0.05$; **: $p < 0.01$; ***: $p < 0.001$) (Reprinted from *Biomaterials*, Vol. 234, He, J.; Qiao, Y.; Zhang, H.; Zhao, J.; Li, W.; Xie, T.; Zhong, D.; Wei, Q.; Hua, S.; Yu, Y.; Yao, K.; Santos, H. A.; Zhou, M. Gold–silver nanoshells promote wound healing from drug-resistant bacteria infection and enable monitoring via surface-enhanced Raman scattering imaging, pp. 119763 (ref 134). Copyright 2020, with permission from Elsevier.). (C-a) Raman imaging of MDA-MB-231 cells incubated with HA-4-ATP-AuNFs. (C-b) Raman spectra of HA-4-ATP-AuNFs at points I and II. (C-c) Cell viabilities of MDA-MB-231 cells with different treatments. * $p < 0.05$; ** $p < 0.01$. (C-d) Fluorescent microscopy images of live/dead MDA-MB-231 cells treated with different conditions with or without NIR laser irradiation (1064 nm, 1 W/cm). Live cells were stained green with calcein-AM, and dead cells were stained red with PI (Reproduced from Gold Nanoframeworks with Mesopores for Raman–Photoacoustic Imaging and Photo-Chemo Tumor Therapy in the Second Near-Infrared Biowindow, Wang, J.; Sun, J.; Wang, Y.; Chou, T.; Zhang, Q.; Zhang, B.; Ren, L.; Wang, H. *Adv. Funct. Mater.*, Vol. 30, Issue 9 (ref 142). Copyright 2020, with permission from Wiley.).

affinity for targeting a nucleolin-specific aptamer, outer SiO₂ shell as a protective shell to ensure the stability, and signal fidelity of encoded AuNCs nanoprobe. The bifunctional nanoprobe successfully exhibited strong and high SERS/photothermal effects in nucleolin-positive breast cancer cells under an NIR laser (Figure 8A).

3.1.2. Photothermal Antimicrobial Therapy. Chronic infection often occurs in the process of wound healing. The complications of the same chronic wound will affect the process of wound healing, which can progress from local infection to systemic infection, sepsis, multiple organ dysfunction, and eventually death. Timely and effective treatments are critical to the patient's recovery. Antibiotics are mainly used to treat various bacterial infections or pathogenic microbial infections

that play an important role in treating bacterial infections. While effective antibiotics achieve good therapeutic results, the abuse of antibiotics often leads to the widespread presence of multidrug-resistant bacteria, which requires people to continue looking for alternative antibiotic treatments for multidrug-resistant bacteria.¹³² With characteristics of remote-controlled and noninvasive therapeutic therapy, photothermal treatment of bacteria has attracted more and more attention in recent years.

It is well-known that Ag ion can adhere to the cell membrane of bacteria to increase the permeability of the cell membrane and then irreversibly interact with thiol groups at various proteins in the cell, leading to the destruction of intracellular enzymes and the death of bacteria.¹³³ To completely eradicate bacteria and inhibit bacterial infection, Zhou and co-workers have developed

a multifunctional gold–silver nanoshell (AuAgNS) nanosystem for *in situ* monitoring of bacterial infectious diseases and verifying the therapeutic effect (Figure 8B).¹³⁴ When AuAg hybrid hollow shell nanoshells with a strong responsiveness to the NIR laser were synthesized, AuAgNSs exhibited an efficient photothermal effect and simultaneously released silver ions during laser irradiation that could wipe out bacteria. Then, when 3,3'-diethylthiatricarbocyanine iodide (DTTC) molecules were coupled onto the shells, the SPR peak of AuAgNSs-DTTC was proximal to the wavelength of the excitation laser for Raman imaging (785 nm). MRSA138 and extended-spectrum β -lactamase *Escherichia coli*, two MDR bacteria strains, were chosen as bacteria models. After ESB *E. coli* or MRSA was incubated with AuAgNSs-DTTC, *in vitro* antibacterial activity of AuAgNSs was observed under an 808 nm laser (1.0 W cm^{-2}). To help keep AuAgNSs on the surface of the wound, nanoparticles were commixed with sodium hyaluronic gel to obtain mixed AuAgNSs. The hybrid AuAgNSs were applied to the wound, and the wound temperature rose by over $20 \text{ }^\circ\text{C}$ within a laser irradiation of 50 s. Eight days after treatment, an immunohistochemical staining (CD31 and IL-1) histological examination was taken. The results demonstrated that photothermal therapy and silver ion release promoted wound healing and reduced inflammatory responses.

However, there are still some challenges to distinguish the nonspecific binding between infection sites and healthy tissues when NIR light energy is converted into localized heat. To effectively eliminate bacterial pathogens that have a noninvasive effect on normal tissues, Jiang and co-workers designed a novel SERS-based platform to provide optimal bacterial SERS imaging and photothermal antibacterial treatment.¹³⁵ In this study, a trans-cyclooctene derivative of vancomycin (Van-TCO) was used to specifically bind to the surface of Gram-positive bacteria on the bacterial cell wall. Then, a kind of tetrazine-modified gold nanoparticle (GNP) reacted orthogonally with Van-TCO to form aggregated GNPs on the surface of the bacteria. When samples were illuminated with an 808 nm NIR laser at 2 W/cm^2 for 5 min, a strong electromagnetic field and high NIR absorption were produced by the plasmon coupling effect between the adjacent GNPs. Since tetrazine modified GNPs had no binding sites of Van-TCO and were formed on the bacterial surface not inside bacterial cells, they dispersed and exhibited no damage to healthy tissues when light energy was converted into localized heat.

3.2. Therapeutic Drug Delivery System. Drug-loaded nanomaterials, known as nanomedicines, have received increasing attention for their ability to personalize therapeutic drugs to improve therapeutic efficacy and reduce side effects.^{136,137} The integration of targeted drug delivery, imaging, and treatment monitoring into a single nanopatform is important for high-performance therapeutics. Integrated nanopatforms in additional studies have demonstrated effective drug accumulation at tumor sites and high photodynamic therapy (PDT) and photothermal therapy (PTT) efficiency, and they have been successfully used for early monitoring and guiding early treatment to achieve tumor elimination. PDT therapy is an emerging therapy that uses photosensitizers to absorb radiant energy. Accompanied by biological effects with the participation of oxygen molecules, highly active singlet oxygen ($^1\text{O}_2$) can oxidize with nearby biological macromolecules to produce cytotoxicity and kill cells in the exposed area.^{138,139} However, due to many technical difficulties, PDT has not been widely used as a general therapy in clinical practice. A major challenge is the

poor solubility of the photosensitizer (PS), which limits the application *in vivo*. Since metallic phthalocyanines are ideal PSs due to their low toxicity and high molar absorption coefficient in the NIR windows, the main challenges of *in vivo* application are poor hydrophilicity and lack of molecular selectivity. To improve solubility and cell uptake, Tian's team used hexagonal boron nitride nanosheets (h-BNNS) as SERS probes and loaded copper(II) phthalocyanine (CuPc) on them to construct a cooperative PS delivery system.¹⁴⁰ CuPc was embedded into hairpin G-quadruplex (HG) DNA to improve its solubility, and CuPc@HG was bound to h-BNNS by π - π stacking to form the CuPc@HG@Bn probe with a loading capacity of about $0.54 \mu\text{mol}$ CuPc per mg. Also, the disadvantage of PDT was that the depth of the laser irradiation was short, which had a poor effect on the tumor with a deep invasion; NIR light with a high penetration depth showed great advantages as the excitation light source. In this study, the CuPc molecules were the PSs and carried out *in situ* monitoring and imaging of miR-21 through CuPc on H-BNNS. Due to the designed miRNA cycle amplification and the high SERS effect of CuPc on H-BNNS, the LOD of miRNA-21 in the cell was down to 0.7 fM under the NIR laser. In this study, the tumor was completely cleared after only 3 days with a low dose ($25 \mu\text{g/mL}$) of drug (CuPc@HG@Bn) when the miR-21 concentration was below 7 fM in the primary stage of the tumor.

The PDT effect of the single drug is limited. In order to improve the antitumor efficacy, the combination of PTT and PDT was studied, and there was evidence that the treatment efficiency was then improved; patients achieved a longer survival time. A common strategy is to integrate a multicomponent photosensitizer (PS) into a nanounit to obtain multiple phototherapies through different light irradiations. However, multiple PSs have interferences by many factors such as complex synthesis processes and possible interactions between them. Prussian blue has significant absorption characteristics in the NIR region. Photosensitizers that can be used simultaneously as photothermal (PT) and photodynamic (PD) therapy show great advantages. Shen and co-workers designed a SERS probe using Prussian blue, a novel low-toxicity MR contrast agent, as the reporter molecule.¹⁴¹ Hyaluronic acid (HA) is also chosen as the packaging agent due to its good water solubility and outstanding active targeting function for the CD44 receptor. The whole mixed material showed excellent biocompatibility and high selectivity to tumors overexpressing the CD44 receptor. Highly targeted tumor ablation efficiency was achieved in real-time tumors of rats through MR and SERS dual-mode imaging capabilities.

Different from PDT therapy, specific tumor chemotherapy drugs are also important for tumor ablation. The targeted selective release of chemotherapeutic drugs can lead to unnecessary injuries being avoided. To improve the depth of tissue that could be treated, Wang et al. developed gold nanoframeworks (AuNFs) with large pores for multiplex imaging and delivery of a cancer-targeted drug.¹⁴² The high hotspot density of the synthetic AuNFs showed a strong absorption for deep tumors in the NIR-II region and provided NIR-II mediated PTT and photoacoustic imaging. Large mesopores in the AuNFs enabled the encapsulation of small molecule cargo and loading of DOX into the mesopores. Raman reporter molecules 4-aminophen (4-ATP) connected to the surface of the AuNFs via thiol groups. Hyaluronic acid (HA), a natural polysaccharide with a high affinity for CD44, as a functional group can target CD44 overexpressed tumor cells by

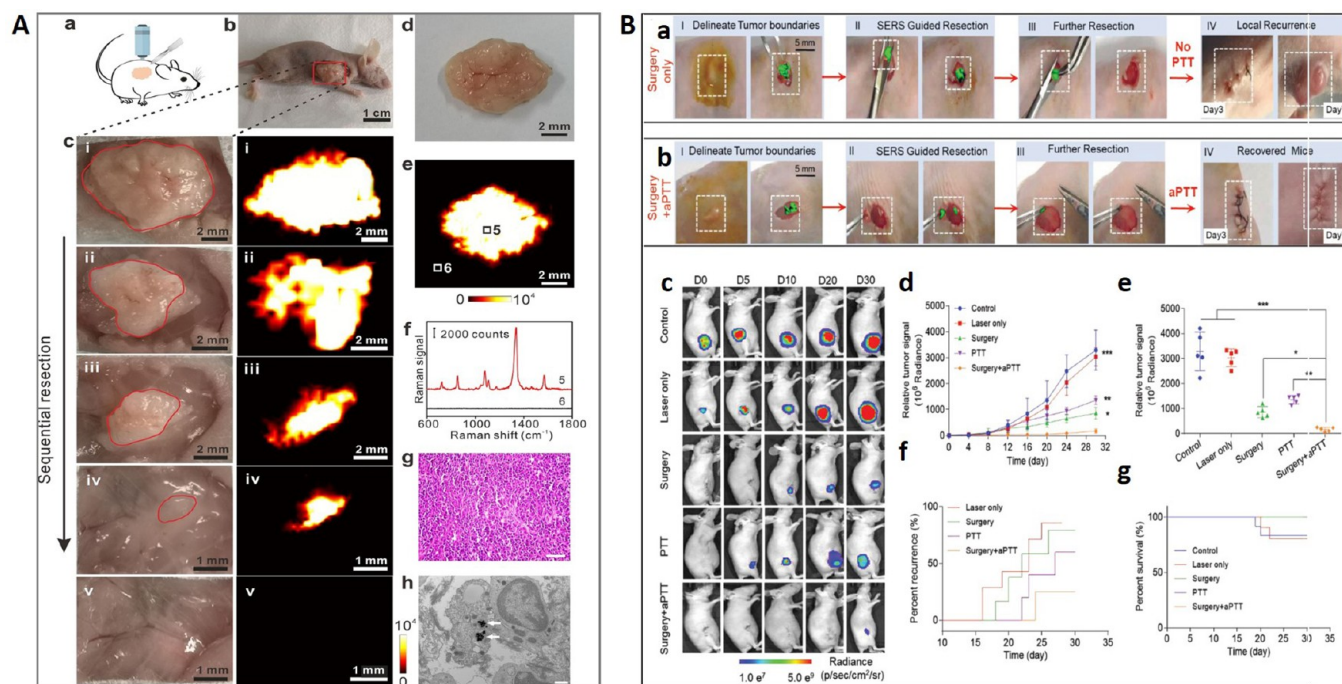


Figure 9. SERS imaging-guided surgery therapy. (A) *In vivo* intraoperative Raman imaging-guided tumor excision and *ex vivo* tumor SERS imaging. (A-a) Cartoon illustration of Raman imaging-guiding tumor resection at 6 h after intravenous injection of Gd-GERTs. (A-b) Photograph of the animal model before tumor excision. The red box indicates the tumor site. (A-c) Photographs (left) and the corresponding Raman images (right) during the sequential tumor resection until the entire tumor had been removed. (A-d) Photograph and (A-e) the corresponding Raman image of a resected gross tumor at 24 h after injection. (A-f) Raman spectra acquired from points 5 and 6, indicated in (A-e). (A-g) H&E staining of the resected tumor. The scale bar is 20 μm . (A-h) TEM image of the tumor tissue. The white arrows indicate the existence of Gd-GERTs. The scale bar is 500 nm (For the interpretation of the references for the colors in this figure legend, the reader is referred to the web version of this article.) (Reprinted from *Acta Biomater.*, Vol. 104, Shi, B.; Zhang, B.; Zhang, Y.; Gu, Y.; Zheng, C.; Yan, J.; Chen, W.; Yan, F.; Ye, J.; Zhang, H. Multifunctional Gap-Enhanced Raman Tags for Preoperative and Intraoperative Cancer Imaging, pp. 210–220 (ref 146). Copyright 2020, with permission from Elsevier.). (B) Raman image-guided resection and adjuvant photothermal therapy (aPTT) of the subcutaneous SKOV3 ovarian tumors. (B-a, B-b) Raman image-guided surgery and with the addition of adjuvant photothermal treatment, respectively (785 nm, 150 mW, 5 \times objective, 0.2 s integration time, and 3–10 min in total). (B-c) Bioluminescent images of the representative mice from 5 different treatment groups. (B-d) Variation of the tumor BLI signals after different treatments. (B-e) Relative tumor signals measured in different groups after 30 days. (B-f) The rate of tumor recurrences in different treatment groups. (B-g) Kaplan–Meier plot showing the rate of mice survival in different groups. *In vivo* bioluminescence images were used to track tumor signals in different groups of mice. Data are presented as the mean \pm SD; *p* values were calculated by Student's *t* test ($n = 5$, ** $p < 0.01$, *** $p < 0.001$, relative to the control mice) (Reproduced with permission from Intraoperative Assessment and Photothermal Ablation of the Tumor Margins Using Gold Nanoparticles. Wei, Q.; Arami, H.; Santos, H. A.; Zhang, H.; Li, Y.; He, J.; Zhong, D.; Ling, D.; Zhou. *Adv. Sci.*, Vol. 8, Issue 5 (ref 150). Copyright 2021, with permission from Wiley).

forming the amide bond between the 4-ATP ammonia of HA to the AuNFs surface for the HA-4-ATP-AuNFs-DOX nanosystem. The directional synthetic AuNF liposomes have high biocompatibility. The photothermal effects of the AuNFs irradiated by the NIR-II laser could relax the HA layer structure and reduce the viscosity of the HA, hence leading to the release of DOX molecules. Almost complete tumor eradication was achieved with PA-Raman dual image-guided photochemotherapy, and the degree of ablation of cancer cells in histopathological sections was verified by HE (Figure 8C).

3.3. SERS Image-Guided Surgery Therapy. In recent years, the elimination of tumor cells by noninvasive SERS image-guided surgery has attracted extensive attention due to narrow SERS spectral peaks and each targeted molecule-specific fingerprint spectrum, opening new ways for ultrahigh and single-cell level resolution imaging on the tissue surface. Meanwhile, SERS imaging can be combined with other imaging methods like photoacoustic and MRI for multimodal imaging to achieve more accurate tumor imaging and excision. In addition, noble metal nanoparticles can quench fluorescence so that fluorescent dyes can be used as Raman reporters. The use of

such Raman reporters is conducive to the further enhancement of SERRS, when the analyte contains chromophore energy close to the excitation radiation. For SERS application *in vivo*, the NIR resonance enhancement between fluorophore as the SERS reporter and the laser source has received extensive attention.¹⁴³

This combination of resonance and surface enhancement enhances up to 10^{14} compared to normal Raman scattering. Yue et al. developed a SERRS probe based on gold nanospheres (AuNSs).¹⁴⁴ They used NIR fluorophore IR783 as the Raman reporters, and FAL peptides of the EGFR-targeted ligand were bound to the ligand-binding site of the probe. Tumor boundaries were defined preoperatively by magnetic resonance imaging (MRI), and glioblastoma boundaries were distinguished from normal cells intraoperatively by SERRS imaging. However, all relevant studies were conducted in isolated mouse brains. In order to evaluate the outcome of SERRS image-guided surgery *in vivo*, the same groups developed gold nanostars as substrates for the SERRS probe to guide glioma resection in live mouse models.¹⁴⁵ MRI was used to locate the xenografts of the *in situ* glioma and design the craniotomy plan. The brain tumor was surgically removed in a live mouse model with the help of a

hand-held Raman scanner to visualize the margins of the intraoperative tumor under the guidance of NIR-SERRS imaging. The tumor cells were completely removed until the Raman signal from the probe disappeared entirely on the resection bed. It was demonstrated that the recurrence rate of gliomas treated with SERRS-guided surgery was significantly lower compared with white-light assisted surgery, validated by the postoperative enhanced MRI results.

Compared with fluorescence imaging, SERS imaging technology needs a longer imaging time, which generally takes several minutes to several hours to obtain Raman images on a large area with SERRS probes. Therefore, it is still necessary to explore Raman probes with large enhancement factors to shorten the irradiation time to obtain the image. Ye's group developed mesoporous silica gadolinium-loaded gap-enhanced Raman probes (Gd-GERTs), which could be used for (CT/MR/SERS) triple-modal imaging (Figure 9A).¹⁴⁶ Due to the advantages of subnanometer core-shell junctions, a significant amplification of the SERS signal was realized. The enhanced SERS signal could considerably shorten the data acquisition time of SERS imaging.^{147–149} In the study, the multifunctional SERS platform provided noninvasive CT/MR imaging function for preoperative tumor recognition as well as an intraoperative real-time SERS imaging function to guide complete tumor resection.

The residual tumor after resection is the leading cause of recurrence. The high-resolution SERS image-guided surgery provides a more accurate resection of the marginal tumor area, which can potentially remove residual tumors and help. However, precise combination therapy such as PTT, PDT, and the release of drugs can better reduce the recurrence rate. Zhou and co-workers designed a multifunctional nanoplateform combined high-resolution SERS image-guided PTT to ablate metastatic microtumors in mice during surgery.¹⁵⁰ Compared with the control group, the simultaneous surgery and PTT under the guidance of SERS imaging increased the survival rate by 75% and significantly delayed tumor recurrence. Also, it was observed that Raman imaging-guided tumor resection of mouse models with SKOV3 ovarian or CT26 colon tumors minimized autofluorescence and phototoxicity under the 785 nm laser as well as helped to detect tumor foci (0.6 mm) hidden below normal tissue (3 mm) after 24 h, which proved that NIR active SERS imaging technology has superiority in detecting signals under the skin and avoiding skin interference (Figure 9B).

4. SUMMARY AND PERSPECTIVE

In general, we reviewed the recent progress of SERS in the NIR window, which was achieved through the combination of different function materials (substrates, Raman reporter molecules, and functional groups). SERS as a powerful analytical platform for biological and biomedical applications showed high specificity and a low LOD due to its advantages of having a narrow width and plasmonic resonance properties. To fully exploit the potential of SERS probes in biomedical applications, nearly decades of exploration and innovation in substrate materials (from noble metal NP to semiconductor and carbon nanotubes) have been researched to develop their biomedical application potential. Besides, the general uses of hybrid SERS substrates provide a novel platform to combine enhanced electromagnetic and chemical properties with various novel materials. On the basis of the fact the combination of resonance and surface enhancement results in a signal enhancement up to 10^{14} , the work of developing Raman reporter molecules whose

absorption maximum resonates with the NIR detection laser has received a great deal of attention and fluorophores are the most potential candidate reporter molecule. Although many different types of mixed substrate materials may not have the significantly high enhancement factor (ca. 10^6) of pure gold or silver substrates, their high affinity for the analyte molecule can increase the number of surface molecules as well as the combination of different packaging layers to improve their hydrophobicity, thereby improving detection sensitivity and selectivity.

Under the conventional short-wavelength excitation light, SERS detection is limited by a limited tissue penetration depth. As the biological window allows the penetration of several tissues of 100 nm in the NIR range, a 785 nm laser was applied first in *in vivo* studies. With the acquisition of the InGaAs CCD, research on the second NIR windows has been explored. In addition, the second NIR window shows further improved detection sensitivity, spatial resolution, and tissue penetration ratio than the first NIR window. Meanwhile, the detection efficiency between 900 and 1000 nm is low, so it is necessary to further develop an efficient CCD detector. Still, there are far fewer optimized reporter molecules for NIR II, and efforts to improve SERS sensitivity have been turned to the development of Raman reporter molecules due to the presence of strong anisotropic resonance particles in NIR II. Due to the functionalization of the surface of the nanoparticles, the synthesis of NIR-responsive SERS probes has been widely developed in clinical practice.

We reviewed the exploration and application of NIR-responsive SERS probes in recent years. Although so much significant progress has been made, there is still a long way to go. In the future, the application of SERS *in vivo* needs to pay more attention to the stability of the composition of SERS nanoparticles in the complex environment of the human body and the importance of monitoring the long-term fate of their particles, including the biological toxicity of the particles and the clearance rate of various organs. We hope that this Review can provide insights for biological and biomedical researchers searching for new sensitive biosensing and bioimaging methods.

AUTHOR INFORMATION

Corresponding Authors

Rui Wang – Key Laboratory of Hainan Trauma and Disaster Rescue, Laboratory of Neurology, The First Affiliated Hospital of Hainan Medical University and Key Laboratory of Emergency and Trauma, Ministry of Education, Key Laboratory of Hainan Functional Materials and Molecular Imaging, College of Pharmacy, College of Emergency and Trauma, Hainan Medical University, Haikou 571199, China; Email: wangrui@hainmc.edu.cn

Fabiao Yu – Key Laboratory of Hainan Trauma and Disaster Rescue, Laboratory of Neurology, The First Affiliated Hospital of Hainan Medical University and Key Laboratory of Emergency and Trauma, Ministry of Education, Key Laboratory of Hainan Functional Materials and Molecular Imaging, College of Pharmacy, College of Emergency and Trauma, Hainan Medical University, Haikou 571199, China; orcid.org/0000-0003-0073-6299; Email: yufabiao@hainmc.edu.cn

Authors

Hui Chen – Key Laboratory of Hainan Trauma and Disaster Rescue, Laboratory of Neurology, The First Affiliated Hospital

of Hainan Medical University and Key Laboratory of Emergency and Trauma, Ministry of Education, Key Laboratory of Hainan Functional Materials and Molecular Imaging, College of Pharmacy, College of Emergency and Trauma, Hainan Medical University, Haikou 571199, China

Ziyi Cheng – Key Laboratory of Hainan Trauma and Disaster Rescue, Laboratory of Neurology, The First Affiliated Hospital of Hainan Medical University and Key Laboratory of Emergency and Trauma, Ministry of Education, Key Laboratory of Hainan Functional Materials and Molecular Imaging, College of Pharmacy, College of Emergency and Trauma, Hainan Medical University, Haikou 571199, China

Xuejun Zhou – Key Laboratory of Hainan Trauma and Disaster Rescue, Laboratory of Neurology, The First Affiliated Hospital of Hainan Medical University and Key Laboratory of Emergency and Trauma, Ministry of Education, Key Laboratory of Hainan Functional Materials and Molecular Imaging, College of Pharmacy, College of Emergency and Trauma, Hainan Medical University, Haikou 571199, China

Complete contact information is available at:

<https://pubs.acs.org/10.1021/acs.analchem.1c03646>

Author Contributions

[‡]H.C. and Z.C. contributed equally.

Notes

The authors declare no competing financial interest.

Biographies

Hui Chen is currently a master candidate, under the guidance of Prof. Fabio Yu at Hainan Medical University, and has been since 2020. She received her bachelor's degree in clinical laboratory medicine at Bengbu Medical College in 2017. From 2017 to 2020, she worked as a medical laboratory technician in the People's Hospital of Qianjiang. Her current research interests focus on the development of functional nanomaterials for SERS bioimaging.

Ziyi Cheng received his Ph.D. degree under the supervision of Professor Jaebum Choo from the Department of Bionanotechnology, Hanyang University, Korea, in 2019. Currently, he is an associate professor at the Institute of Functional Materials and Molecular Imaging, Hainan Medical University. His research interests focus on surface-enhanced Raman scattering-based microfluidic devices and POCT.

Xuejun Zhou received his bachelor's degree in clinical medicine at Hainan University in 1992. Then, he joined the First Affiliated Hospital of Hainan Medical University. He received his Ph.D. degree in clinical medicine at Southern Medical University in 2016. Currently, he is a professor and the director of Otorhinolaryngology Head and Neck Surgery. His research interests focus on precision treatment of head and neck tumors and intraoperative real-time navigation technology.

Rui Wang received his Ph.D. degree under the supervision of Professor Jaebum Choo from the Department of Bionanotechnology, Hanyang University, Korea, in February 2018. Then, he joined Hainan Medical University in March 2018. Currently, he is an associate professor at the Institute of Functional Materials and Molecular Imaging, Hainan Medical University. His research interests focus on surface-enhanced Raman scattering (SERS) imaging and functional bionanomaterials.

Fabiao Yu is now a full professor at the Key Laboratory of Hainan Functional Materials and Molecular Imaging, Hainan Medical University. He received the Hainan Hundred Talents and Hainan Leading Talents award. After obtaining his M.S. degree from Shandong Normal University in 2009, he received his Ph.D. degree from Dalian University of Technology and Dalian Institute of Chemical Physics, Chinese Academy of Sciences, in 2013. After four years of work at

Yantai Institute of Coastal Zone Research, Chinese Academy of Sciences, he joined the Hainan Medical University in 2018. His research interests focus on functional biomaterials, optical molecular imaging, and disease point-of-care testing.

ACKNOWLEDGMENTS

This work was supported by the National Natural Science Foundation of China (Nos. 21864011, 22064009, and 21775162), Hainan Provincial Natural Science Foundation of China (Nos. 2019RC220, 820RC641, 2019RC210, and 819MS121), Hainan Key Research and Development Project (Grant ZDYF2020133), Natural Science Research Talent Project of Hainan Medical University (Grant JBGS202101), Hainan Province Clinical Medical Center (2021), Nanhai Young-Talent Program of Hainan (20202007), and Hundred Talent Program of Hainan (2018).

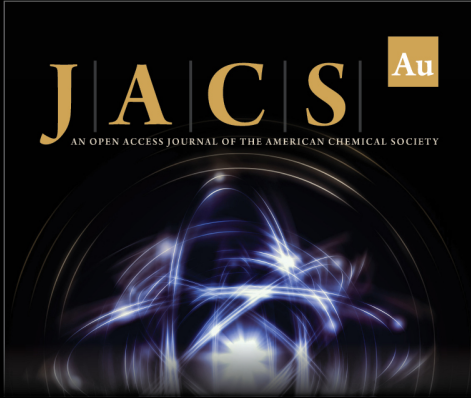
REFERENCES

- (1) Di Mascio, P.; Martinez, G. R.; Miyamoto, S.; Ronsein, G. E.; Medeiros, M. H. G.; Cadet, J. *Chem. Rev.* **2019**, *119* (3), 2043–2086.
- (2) Song, Y.; Sandford, E.; Tian, Y.; Yin, Q.; Kozminski, A. G.; Su, S.-H.; Cai, T.; Ye, Y.; Chung, M. T.; Lindstrom, R.; Goicochea, A.; Barabas, J.; Olesnavich, M.; Rozwadowski, M.; Li, Y.; Alam, H. B.; Singer, B. H.; Ghosh, M.; Choi, S. W.; Tewari, M.; Kurabayashi, K. *Blood* **2021**, *137* (12), 1591–1602.
- (3) Bruch, R.; Baaske, J.; Chatelle, C.; Meirich, M.; Madlener, S.; Weber, W.; Dincer, C.; Urban, G. A. *Adv. Mater.* **2019**, *31* (51), 1905311.
- (4) Lv, J.; Peng, Y.; Li, S.; Guo, Z.; Zhao, Q.; Zhang, X.; Nie, L. *Eur. Radiol.* **2018**, *28* (5), 2176–2183.
- (5) Liu, Y.; Kim, M.; Cho, S. H.; Jung, Y. S. *Nano Today* **2021**, *37*, 101063.
- (6) Langer, J.; Jimenez de Aberasturi, D.; Aizpurua, J.; Alvarez-Puebla, R. A.; Auguie, B.; Baumberg, J. J.; Bazan, G. C.; Bell, S. E. J.; Boisen, A.; Brolo, A. G.; Choo, J.; Cialla-May, D.; Deckert, V.; Fabris, L.; Faulds, K.; Garcia de Abajo, F. J.; Goodacre, R.; Graham, D.; Haes, A. J.; Haynes, C. L.; Huck, C.; Itoh, T.; Kall, M.; Kneipp, J.; Kotov, N. A.; Kuang, H.; Le Ru, E. C.; Lee, H. K.; Li, J. F.; Ling, X. Y.; Maier, S. A.; Mayerhofer, T.; Moskovits, M.; Murakoshi, K.; Nam, J. M.; Nie, S.; Ozaki, Y.; Pastoriza-Santos, I.; Perez-Juste, J.; Popp, J.; Pucci, A.; Reich, S.; Ren, B.; Schatz, G. C.; Shegai, T.; Schlucker, S.; Tay, L. L.; Thomas, K. G.; Tian, Z. Q.; Van Duyne, R. P.; Vo-Dinh, T.; Wang, Y.; Willets, K. A.; Xu, C.; Xu, H.; Xu, Y.; Yamamoto, Y. S.; Zhao, B.; Liz-Marzan, L. M. *ACS Nano* **2020**, *14* (1), 28–117.
- (7) Cialla-May, D.; Zheng, X. S.; Weber, K.; Popp, J. *Chem. Soc. Rev.* **2017**, *46* (13), 3945–3961.
- (8) dos Santos, D. P.; Temperini, M. L. A.; Brolo, A. G. *Acc. Chem. Res.* **2019**, *52* (2), 456–464.
- (9) Li, J.; Wuethrich, A.; Sina, A. A. I.; Cheng, H. H.; Wang, Y.; Behren, A.; Mainwaring, P. N.; Trau, M. *Nat. Commun.* **2021**, *12* (1), 1087.
- (10) Shan, B.; Pu, Y.; Chen, Y.; Liao, M.; Li, M. *Coord. Chem. Rev.* **2018**, *371*, 11–37.
- (11) Xu, K.; Zhou, R.; Takei, K.; Hong, M. *Adv. Sci.* **2019**, *6* (16), 1900925.
- (12) Zong, C.; Xu, M.; Xu, L. J.; Wei, T.; Ma, X.; Zheng, X. S.; Hu, R.; Ren, B. *Chem. Rev.* **2018**, *118* (10), 4946–4980.
- (13) Hong, G. S.; Antaris, A. L.; Dai, H. J. *Nat. Biomed.* **2017**, *1* (1), 0010.
- (14) Lane, L. A.; Xue, R.; Nie, S. *Curr. Opin. Chem. Biol.* **2018**, *45*, 95–103.
- (15) Cai, Y.; Wei, Z.; Song, C.; Tang, C.; Han, W.; Dong, X. *Chem. Soc. Rev.* **2019**, *48* (1), 22–37.
- (16) Gong, H.; Peng, R.; Liu, Z. *Adv. Drug Delivery Rev.* **2013**, *65* (15), 1951–1963.
- (17) Wu, D.; Xue, D.; Zhou, J.; Wang, Y.; Feng, Z.; Xu, J.; Lin, H.; Qian, J.; Cai, X. *Theranostics* **2020**, *10* (8), 3636–3651.

- (18) Yu, Q.; Wang, Y.; Mei, R.; Yin, Y.; You, J.; Chen, L. *Anal. Chem.* **2019**, *91* (8), 5270–5277.
- (19) Ding, S. Y.; You, E. M.; Tian, Z. Q.; Moskovits, M. *Chem. Soc. Rev.* **2017**, *46* (13), 4042–4076.
- (20) Kenry; Duan, Y.; Liu, B. *Adv. Mater.* **2018**, *30* (47), 1802394.
- (21) Shan, B.; Li, L.; Zhao, Y.; Wang, H.; Li, M. *Adv. Funct. Mater.* **2021**, *31* (29), 2103186.
- (22) He, M.-Q.; Yu, Y.-L.; Wang, J.-H. *Nano Today* **2020**, *35*, 101005.
- (23) Solís, D. M.; Taboada, J. M.; Obelleiro, F.; Liz-Marzán, L. M.; García de Abajo, F. J. *ACS Photonics* **2017**, *4* (2), 329–337.
- (24) Tao, L.; Chen, K.; Chen, Z.; Cong, C.; Qiu, C.; Chen, J.; Wang, X.; Chen, H.; Yu, T.; Xie, W.; Deng, S.; Xu, J. B. *J. Am. Chem. Soc.* **2018**, *140* (28), 8696–8704.
- (25) Yang, Y.; Cong, Y.; Shang, J.; Liu, Y.; Fang, G.; Zhang, J.; Dong, B. *Sens. Actuators, B* **2021**, *330*, 129199.
- (26) Park, S.; Lee, J.; Ko, H. *ACS Appl. Mater. Interfaces* **2017**, *9* (50), 44088–44095.
- (27) Zhu, X.; Jia, H.; Zhu, X.-M.; Cheng, S.; Zhuo, X.; Qin, F.; Yang, Z.; Wang, J. *Adv. Funct. Mater.* **2017**, *27* (22), 1700016.
- (28) Pal, S.; Ray, A.; Andreou, C.; Zhou, Y.; Rakshit, T.; Włodarczyk, M.; Maeda, M.; Toledo-Crow, R.; Berisha, N.; Yang, J.; Hsu, H.-T.; Oseledchik, A.; Mondal, J.; Zou, S.; Kircher, M. F. *Nat. Commun.* **2019**, *10* (1), 1926.
- (29) Zhuo, X.; Henriksen-Lacey, M.; Jimenez de Aberasturi, D.; Sanchez-Iglesias, A.; Liz-Marzán, L. M. *Chem. Mater.* **2020**, *32* (13), 5879–5889.
- (30) Huang, S.; He, Y.; Yang, X.; Yuan, R.; Chai, Y. *Sens. Actuators, B* **2020**, *304*, 127273.
- (31) He, J.; Qiao, Y.; Zhang, H.; Zhao, J.; Li, W.; Xie, T.; Zhong, D.; Wei, Q.; Hua, S.; Yu, Y.; Yao, K.; Santos, H. A.; Zhou, M. *Biomaterials* **2020**, *234*, 119763.
- (32) Gao, Y.; Wu, W.; Qiao, K.; Feng, J.; Zhu, L.; Zhu, X. *Water Res.* **2021**, *204*, 117603.
- (33) Anker, J. N.; Hall, W. P.; Lyandres, O.; Shah, N. C.; Zhao, J.; Van Duyne, R. P. *Nat. Mater.* **2008**, *7* (6), 442–453.
- (34) von Maltzahn, G.; Centrone, A.; Park, J.; Ramanathan, R.; Sailor, M.; Hatton, T.; Bhatia, S. *Adv. Mater.* **2009**, *21* (31), 3175–3180.
- (35) Li, K.; Tang, X.; Liu, G.; Mi, J.; Du, J.; Huang, W.; Zuo, Z.; Lu, Y. *Appl. Surf. Sci.* **2021**, *570*, 151069.
- (36) Meng, X.; Dyer, J.; Huo, Y.; Jiang, C. *Langmuir* **2020**, *36* (13), 3558–3564.
- (37) Senthil Kumar, P.; Pastoriza-Santos, I.; Rodríguez-González, B.; Javier García de Abajo, F.; Liz-Marzán, L. M. *Nanotechnology* **2008**, *19* (1), No. 015606.
- (38) Jimenez de Aberasturi, D.; Serrano-Montes, A. B.; Langer, J.; Henriksen-Lacey, M.; Parak, W. J.; Liz-Marzán, L. M. *Chem. Mater.* **2016**, *28* (18), 6779–6790.
- (39) Lee, H. K.; Lee, Y. H.; Koh, C. S. L.; Phan-Quang, G. C.; Han, X.; Lay, C. L.; Sim, H. Y. F.; Kao, Y. C.; An, Q.; Ling, X. Y. *Chem. Soc. Rev.* **2019**, *48* (3), 731–756.
- (40) Gurbatov, S. O.; Modin, E.; Puzikov, V.; Tonkaev, P.; Storozhenko, D.; Sergeev, A.; Mintcheva, N.; Yamaguchi, S.; Tarasenko, N. N.; Chuvilin, A.; Makarov, S.; Kulinich, S. A.; Kuchmizhak, A. A. *ACS Appl. Mater. Interfaces* **2021**, *13* (5), 6522–6531.
- (41) Zhao, X.; Liu, C.; Yu, J.; Li, Z.; Liu, L.; Li, C.; Xu, S.; Li, W.; Man, B.; Zhang, C. *Nanophotonics* **2020**, *9* (16), 4761–4773.
- (42) Yang, L.; Peng, Y.; Yang, Y.; Liu, J.; Li, Z.; Ma, Y.; Zhang, Z.; Wei, Y.; Li, S.; Huang, Z.; Long, N. V. *ACS Appl. Nano Mater.* **2018**, *1* (9), 4516–4527.
- (43) Lombardi, J. R.; Birke, R. L. *J. Phys. Chem. C* **2014**, *118* (20), 11120–11130.
- (44) Lin, J.; Yu, J.; Akakuru, O. U.; Wang, X.; Yuan, B.; Chen, T.; Guo, L.; Wu, A. *Chem. Sci.* **2020**, *11* (35), 9414–9420.
- (45) Yang, L.; Peng, Y.; Yang, Y.; Liu, J.; Huang, H.; Yu, B.; Zhao, J.; Lu, Y.; Huang, Z.; Li, Z.; Lombardi, J. R. *Adv. Sci.* **2019**, *6* (12), 1970070.
- (46) Yang, L.; Peng, Y.; Yang, Y.; Liu, J.; Huang, H.; Yu, B.; Zhao, J.; Lu, Y.; Huang, Z.; Li, Z.; Lombardi, J. R. *Adv. Sci.* **2019**, *6* (12), 1900310.
- (47) Li, A.; Lin, J.; Huang, Z.; Wang, X.; Guo, L. *iScience* **2018**, *10*, 1–10.
- (48) Lin, J.; Ren, W.; Li, A.; Yao, C.; Chen, T.; Ma, X.; Wang, X.; Wu, A. *ACS Appl. Mater. Interfaces* **2020**, *12* (4), 4204–4211.
- (49) Zhou, L.; Zhou, J.; Lai, W.; Yang, X.; Meng, J.; Su, L.; Gu, C.; Jiang, T.; Pun, E. Y. B.; Shao, L.; Petti, L.; Sun, X. W.; Jia, Z.; Li, Q.; Han, J.; Mormile, P. *Nat. Commun.* **2020**, *11* (1), 1785.
- (50) Yu, H.; Zhuang, Z.; Li, D.; Guo, Y.; Li, Y.; Zhong, H.; Xiong, H.; Liu, Z.; Guo, Z. *J. Mater. Chem. B* **2020**, *8* (5), 1040–1048.
- (51) Zavaleta, C. L.; Smith, B. R.; Walton, I.; Doering, W.; Davis, G.; Shojaei, B.; Natan, M. J.; Gambhir, S. S. *Proc. Natl. Acad. Sci. U. S. A.* **2009**, *106* (32), 13511–13516.
- (52) Rao, A. M.; Richter, E.; Bandow, S.; Chase, B.; Eklund, P. C.; Williams, K.; Fang, S.; Subbaswamy, K. R.; Menon, M.; Thess, A.; Smalley, R. E.; Dresselhaus, G.; Dresselhaus, M. S. *Science* **1997**, *275*, 187–191.
- (53) Liu, Z.; Li, X.; Tabakman, S. M.; Jiang, K.; Fan, S.; Dai, H. *J. Am. Chem. Soc.* **2008**, *130* (41), 13540–13541.
- (54) Habibullah, G.; Viktorova, J.; Ruml, T. *Nanoscale Res. Lett.* **2021**, *16* (1), 47.
- (55) Heller, D. A.; Baik, S.; Eurell, T. E.; Strano, M. S. *Adv. Mater.* **2005**, *17* (23), 2793–2799.
- (56) Kang, J. W.; Nguyen, F. T.; Lue, N.; Dasari, R. R.; Heller, D. A. *Nano Lett.* **2012**, *12* (12), 6170–6174.
- (57) Liu, Z.; Tabakman, S.; Sherlock, S.; Li, X.; Chen, Z.; Jiang, K.; Fan, S.; Dai, H. *Nano Res.* **2010**, *3* (3), 222–233.
- (58) Wang, X.; Wang, C.; Cheng, L.; Lee, S.-T.; Liu, Z. *J. Am. Chem. Soc.* **2012**, *134* (17), 7414–7422.
- (59) Qin, X.; Si, Y.; Wang, D.; Wu, Z.; Li, J.; Yin, Y. *Anal. Chem.* **2019**, *91* (7), 4529–4536.
- (60) McNay, G.; Eustace, D.; Smith, W. E.; Faulds, K.; Graham, D. *Appl. Spectrosc.* **2011**, *65* (8), 825–837.
- (61) Chen, J.; Sheng, Z.; Li, P.; Wu, M.; Zhang, N.; Yu, X. F.; Wang, Y.; Hu, D.; Zheng, H.; Wang, G. P. *Nanoscale* **2017**, *9* (33), 11888–11901.
- (62) Xu, L.; Zhao, S.; Ma, W.; Wu, X.; Li, S.; Kuang, H.; Wang, L.; Xu, C. *Adv. Funct. Mater.* **2016**, *26* (10), 1602–1608.
- (63) Adarsh, N.; Ramya, A. N.; Maiti, K. K.; Ramaiah, D. *Chem. - Eur. J.* **2017**, *23* (57), 14286–14291.
- (64) Harmsen, S.; Huang, R.; Wall, M. A.; Karabeber, H.; Samii, J. M.; Spaliviero, M.; White, J. R.; Monette, S.; O'Connor, R.; Pitter, K. L.; Sastra, S. A.; Saborowski, M.; Holland, E. C.; Singer, S.; Olive, K. P.; Lowe, S. W.; Blasberg, R. G.; Kircher, M. F. *Sci. Transl. Med.* **2015**, *7* (271), 271ra7.
- (65) Li, S.; Pedano, M. L.; Chang, S. H.; Mirkin, C. A.; Schatz, G. C. *Nano Lett.* **2010**, *10* (5), 1722–1727.
- (66) Ma, Y.; Promthaveepong, K.; Li, N. *Adv. Opt. Mater.* **2017**, *5* (14), 1700133.
- (67) Jin, X.; Khlebtsov, B. N.; Khanadeev, V. A.; Khlebtsov, N. G.; Ye, J. *ACS Appl. Mater. Interfaces* **2017**, *9* (36), 30387–30397.
- (68) Choi, N.; Dang, H.; Das, A.; Sim, M. S.; Chung, I. Y.; Choo, J. *Biosens. Bioelectron.* **2020**, *164*, 112326.
- (69) Yin, Y.; Mei, R.; Wang, Y.; Zhao, X.; Yu, Q.; Liu, W.; Chen, L. *Anal. Chem.* **2020**, *92* (21), 14814–14821.
- (70) Andreou, C.; Neuschmelting, V.; Tschaharganeh, D. F.; Huang, C. H.; Oseledchik, A.; Iacono, P.; Karabeber, H.; Colen, R. R.; Mannelli, L.; Lowe, S. W.; Kircher, M. F. *ACS Nano* **2016**, *10* (5), 5015–5026.
- (71) Yue, J.; Liu, Z.; Cai, X.; Ding, X.; Chen, S.; Tao, K.; Zhao, T. *Talanta* **2016**, *150*, 503–509.
- (72) Chen, M.; Zhang, L.; Gao, M.; Zhang, X. *Talanta* **2017**, *172*, 176–181.
- (73) Song, J.; Yang, X.; Yang, Z.; Lin, L.; Liu, Y.; Zhou, Z.; Shen, Z.; Yu, G.; Dai, Y.; Jacobson, O.; Munasinghe, J.; Yung, B.; Peng, G.-J.; Chen, X. *ACS Nano* **2017**, *11* (6), 6102–6113.

- (74) Liang, L.; Zheng, P.; Zhang, C.; Barman, I. *Adv. Mater.* **2021**, *33* (7), 2005133.
- (75) Iacono, P.; Karabeber, H.; Kircher, M. F. *Angew. Chem., Int. Ed.* **2014**, *53* (44), 11756–11761.
- (76) Wang, X.; Wang, C.; Cheng, L.; Lee, S. T.; Liu, Z. *J. Am. Chem. Soc.* **2012**, *134* (17), 7414–7422.
- (77) Gu, X.; Wang, K.; Qiu, J.; Wang, Y.; Tian, S.; He, Z.; Zong, R.; Kraatz, H.-B. *Sens. Actuators, B* **2021**, *334*, 129674.
- (78) Wu, Q.; Chen, G.; Qiu, S.; Feng, S.; Lin, D. *Nanoscale* **2021**, *13* (16), 7574–7582.
- (79) Huang, Y.; Xie, T.; Zou, K.; Gu, Y.; Yang, G.; Zhang, F.; Qu, L.-L.; Yang, S. *Nanoscale* **2021**, *13* (31), 13344–13352.
- (80) Kang, H.; Jeong, S.; Jo, A.; Chang, H.; Yang, J.-K.; Jeong, C.; Kyeong, S.; Lee, Y. W.; Samanta, A.; Maiti, K. K.; Cha, M. G.; Kim, T. K.; Lee, S.; Jun, B. H.; Chang, Y. T.; Chung, J.; Lee, H. Y.; Jeong, D. H.; Lee, Y. S. *Adv. Healthcare Mater.* **2018**, *7* (4), 1700870.
- (81) Qian, X.; Peng, X.-H.; Ansari, D. O.; Yin-Goen, Q.; Chen, G. Z.; Shin, D. M.; Yang, L.; Young, A. N.; Wang, M. D.; Nie, S. *Nat. Biotechnol.* **2008**, *26* (1), 83–90.
- (82) Jambrec, D.; Conzuelo, F.; Zhao, B.; Schuhmann, W. *Electrochim. Acta* **2018**, *276*, 233–239.
- (83) Yang, L.; Peng, Y.; Yang, Y.; Liu, J.; Huang, H.; Yu, B.; Zhao, J.; Lu, Y.; Huang, Z.; Li, Z.; Lombardi, J. R. *Adv. Sci.* **2019**, *6* (12), 1900310.
- (84) Wang, X.; Guo, L. *Angew. Chem., Int. Ed.* **2020**, *59* (11), 4231–4239.
- (85) Demirel, G.; Gieseking, R. L. M.; Ozdemir, R.; Kahmann, S.; Loi, M. A.; Schatz, G. C.; Facchetti, A.; Usta, H. *Nat. Commun.* **2019**, *10* (1), 5502.
- (86) Tian, S.; Neumann, O.; McClain, M. J.; Yang, X.; Zhou, L.; Zhang, C.; Nordlander, P.; Halas, N. J. *Nano Lett.* **2017**, *17* (8), 5071–5077.
- (87) Ganesh, S.; Venkatakrishnan, K.; Tan, B. *Nat. Commun.* **2020**, *11* (1), 1135.
- (88) Thorat, N. D.; Dworniczek, E.; Brennan, G.; Chodaczek, G.; Mouras, R.; Gascón Pérez, V.; Silien, C.; Tofail, S. A. M.; Bauer, J. J. *Mater. Chem. B* **2021**, *9* (3), 846–856.
- (89) Pang, Y.; Li, Q.; Wang, C.; Zhen, S.; Sun, Z.; Xiao, R. *Chem. Eng. J.* **2022**, *429*, 132109.
- (90) Chen, L.; Zhang, Q.; Liu, W.; Xiao, H.; Liu, X.; Fan, L.; Wang, Y.; Li, H.; Cao, C. *Biosens. Bioelectron.* **2021**, *171*, 112676.
- (91) Luo, G.; Zhang, J.; Zhang, S.; Hu, B.; Hu, L.; Huang, Z. *Talanta* **2021**, *224*, 121850.
- (92) Miao, P.; Tang, Y. *Anal. Chem.* **2020**, *92* (17), 12026–12032.
- (93) Zhou, W.; Tian, Y. F.; Yin, B. C.; Ye, B. C. *Anal. Chem.* **2017**, *89* (11), 6120–6128.
- (94) Cheng, Z.; Wang, R.; Xing, Y.; Zhao, L.; Choo, J.; Yu, F. *Analyst* **2019**, *144* (22), 6533–6540.
- (95) Lv, H.; Li, Y.; Zhang, X.; Gao, Z.; Zhang, C.; Zhang, S.; Dong, Y. *Biosens. Bioelectron.* **2018**, *112*, 1–7.
- (96) Zhang, D.; Huang, L.; Liu, B.; Ni, H.; Sun, L.; Su, E.; Chen, H.; Gu, Z.; Zhao, X. *Biosens. Bioelectron.* **2018**, *106*, 204–211.
- (97) Kang, H.; Jeong, S.; Jo, A.; Chang, H.; Yang, J. K.; Jeong, C.; Kyeong, S.; Lee, Y. W.; Samanta, A.; Maiti, K. K.; Cha, M. G.; Kim, T. K.; Lee, S.; Jun, B. H.; Chang, Y. T.; Chung, J.; Lee, H. Y.; Jeong, D. H.; Lee, Y. S. *Adv. Healthcare Mater.* **2018**, *7*, 1700870.
- (98) Li, X.; Niu, G.; Tian, M.; Lu, Q.; Cui, Y.; Yu, X. *Anal. Chem.* **2021**, *93* (26), 9074–9082.
- (99) Liu, S. L.; Sheng, R.; Jung, J. H.; Wang, L.; Stec, E.; O'Connor, M. J.; Song, S.; Bikkavilli, R. K.; Winn, R. A.; Lee, D.; Baek, K.; Ueda, K.; Levitan, I.; Kim, K. P.; Cho, W. *Nat. Chem. Biol.* **2017**, *13* (3), 268–274.
- (100) Courtney, K. C.; Fung, K. Y.; Maxfield, F. R.; Fairn, G. D.; Zha, X. *eLife* **2018**, *7*, e38493.
- (101) Shen, W.; Lin, X.; Jiang, C.; Li, C.; Lin, H.; Huang, J.; Wang, S.; Liu, G.; Yan, X.; Zhong, Q.; Ren, B. *Angew. Chem., Int. Ed.* **2015**, *54* (25), 7308–7312.
- (102) Jiang, X.; Tan, Z.; Lin, L.; He, J.; He, C.; Thackray, B. D.; Zhang, Y.; Ye, J. *Small Methods* **2018**, *2* (11), 1800182.
- (103) Xu, J. J.; Jiang, D. P.; Qin, Y. L.; Xia, J.; Jiang, D. C.; Chen, H. Y. *Anal. Chem.* **2017**, *89* (4), 2216–2220.
- (104) Zhao, S.; Zang, G.; Zhang, Y.; Liu, H.; Wang, N.; Cai, S.; Durkan, C.; Xie, G.; Wang, G. *Biosens. Bioelectron.* **2021**, *179*, 113052.
- (105) Li, D. W.; Chen, H. Y.; Gan, Z. F.; Sun, J. J.; Guo, D.; Qu, L. L. *Sens. Actuators, B* **2018**, *277*, 8–13.
- (106) Chen, H. Y.; Guo, D.; Gan, Z. F.; Jiang, L.; Chang, S.; Li, D.-W. *Microchim. Acta* **2019**, *186* (1), 11.
- (107) Chen, H. Y.; Kouadio Fodjo, E.; Jiang, L.; Chang, S.; Li, J. B.; Zhan, D. S.; Gu, H. X.; Li, D. W. *ACS Sens.* **2019**, *4* (12), 3234–3239.
- (108) Hatfield, K. O.; Gole, M. T.; Schorr, N. B.; Murphy, C. J.; Rodríguez-López, J. *Anal. Chem.* **2021**, *93* (22), 7792–7796.
- (109) Kim, J. A.; Wales, D. J.; Thompson, A. J.; Yang, G. Z. *Adv. Opt. Mater.* **2020**, *8* (9), 1901934.
- (110) Zhang, Y.; Jimenez de Aberasturi, D.; Henriksen-Lacey, M.; Langer, J.; Liz-Marzán, L. M. *ACS Sens.* **2020**, *5* (10), 3194–3206.
- (111) Li, L.; Liang, Y.; Kang, L.; Liu, Y.; Gao, S.; Chen, S.; Li, Y.; You, W.; Dong, Q.; Hong, T.; Yan, Z.; Jin, S.; Wang, T.; Zhao, W.; Mai, H.; Huang, J.; Han, X.; Ji, Q.; Song, Q.; Yang, C.; Zhao, S.; Xu, X.; Ye, Q. *Cancer Cell* **2018**, *33* (3), 368–385.
- (112) Duan, W.; Yue, Q.; Liu, Y.; Zhang, Y.; Guo, Q.; Wang, C.; Yin, S.; Fan, D.; Xu, W.; Zhuang, J.; Gong, J.; Li, X.; Huang, R.; Chen, L.; Aime, S.; Wang, Z.; Feng, J.; Mao, Y.; Zhang, X. Y.; Li, C. *Chem. Sci.* **2020**, *11* (17), 4397–4402.
- (113) Sebba, D.; Lastovich, A. G.; Kuroda, M.; Fallows, E.; Johnson, J.; Ahouidi, A.; Honko, A. N.; Fu, H.; Nielson, R.; Carruthers, E.; Diedhiou, C.; Ahmadou, D.; Soropogui, B.; Ruedas, J.; Peters, K.; Bartkowiak, M.; Magassouba, N.; Mboup, S.; Ben Amor, Y.; Connor, J. H.; Weidemaier, K. *Sci. Transl. Med.* **2018**, *10* (471), eaat0944.
- (114) Wang, C.; Mu, X.; Huo, J.; Zhang, B.; Zhang, K. *Microsyst. Technol.* **2021**, *27* (9), 3285–3291.
- (115) Chattopadhyay, S.; Sabharwal, P. K.; Jain, S.; Kaur, A.; Singh, H. *Anal. Chim. Acta* **2019**, *1067*, 98–106.
- (116) Zhu, W.; Wang, C.-Y.; Hu, J.-M.; Shen, A.-G. *Anal. Chem.* **2021**, *93* (11), 4876–4883.
- (117) Adamczyk, A.; Matuszyk, E.; Radwan, B.; Rocchetti, S.; Chlopicki, S.; Baranska, M. *J. Med. Chem.* **2021**, *64* (8), 4396–4409.
- (118) Strozzyk, M. S.; de Aberasturi, D. J.; Gregory, J. V.; Brust, M.; Lahann, J.; Liz-Marzán, L. M. *Adv. Funct. Mater.* **2017**, *27* (33), 1701626.
- (119) De Marchi, S.; Bodelón, G.; Vázquez-Iglesias, L.; Liz-Marzán, L. M.; Pérez-Juste, J.; Pastoriza-Santos, I. *Appl. Mater. Today* **2019**, *14*, 207–215.
- (120) Jimenez de Aberasturi, D.; Henriksen-Lacey, M.; Litt, L.; Langer, J.; Liz-Marzán, L. M. *Adv. Funct. Mater.* **2020**, *30* (14), 1909655.
- (121) Gravely, M.; Roxbury, D. *ACS Nano* **2021**, *15* (7), 12388–12404.
- (122) Shao, D.; Zhang, X.; Liu, W.; Zhang, F.; Zheng, X.; Qiao, P.; Li, J.; Dong, W. f.; Chen, L. *ACS Appl. Mater. Interfaces* **2016**, *8* (7), 4303–4308.
- (123) Yuan, Y.; Raj, P.; Zhang, J.; Siddhanta, S.; Barman, I.; Bulte, J. W. M. *Angew. Chem., Int. Ed.* **2021**, *60* (8), 3923–3927.
- (124) Yang, L.; Kim, T. H.; Cho, H. Y.; Luo, J.; Lee, J. M.; Chueng, S. T. D.; Hou, Y.; Yin, P. T. T.; Han, J.; Kim, J. H.; Chung, B. G.; Choi, J. W.; Lee, K. B. *Adv. Funct. Mater.* **2021**, *31* (5), 2006918.
- (125) Dey, P.; Tabish, T. A.; Mosca, S.; Palombo, F.; Matousek, P.; Stone, N. *Small* **2020**, *16* (10), 1906780.
- (126) del Valle, A. C.; Yeh, C.-K.; Huang, Y.-F. *Adv. Healthcare Mater.* **2020**, *9* (20), 2070074.
- (127) Guo, W.; Johnston-Peck, A. C.; Zhang, Y.; Hu, Y.; Huang, J.; Wei, W. D. *J. Am. Chem. Soc.* **2020**, *142* (25), 10921–10925.
- (128) Zhang, W.; Liu, J.; Niu, W.; Yan, H.; Lu, X.; Liu, B. *ACS Appl. Mater. Interfaces* **2018**, *10* (17), 14850–14856.
- (129) Song, C.; Li, F.; Guo, X.; Chen, W.; Dong, C.; Zhang, J.; Zhang, J.; Wang, L. *J. Mater. Chem. B* **2019**, *7* (12), 2001–2008.
- (130) Qiu, J.; Xie, M.; Wu, T.; Qin, D.; Xia, Y. *Chem. Sci.* **2020**, *11* (48), 12955–12973.

- (131) Wen, S.; Miao, X.; Fan, G. C.; Xu, T.; Jiang, L. P.; Wu, P.; Cai, C.; Zhu, J. J. *ACS Sens.* **2019**, *4* (2), 301–308.
- (132) Elliott, A. G.; Huang, J. X.; Neve, S.; Zuegg, J.; Edwards, I. A.; Cain, A. K.; Boinett, C. J.; Barquist, L.; Lundberg, C. V.; Steen, J.; Butler, M. S.; Mobli, M.; Porter, K. M.; Blaskovich, M. A. T.; Lociuoro, S.; Strandh, M.; Cooper, M. A. *Nat. Commun.* **2020**, *11* (1), 3184.
- (133) Dong, L. J.; Lai, Y. J.; Yu, S. J.; Liu, J. F. *Anal. Chem.* **2019**, *91* (19), 12525–12530.
- (134) He, J.; Qiao, Y.; Zhang, H.; Zhao, J.; Li, W.; Xie, T.; Zhong, D.; Wei, Q.; Hua, S.; Yu, Y.; Yao, K.; Santos, H. A.; Zhou, M. *Biomaterials* **2020**, *234*, 119763.
- (135) Wang, H.; Ouyang, W.; Zhang, X.; Xue, J.; Lou, X.; Fan, R.; Zhao, X.; Shan, L.; Jiang, T. *J. Mater. Chem. B* **2019**, *7* (30), 4630–4637.
- (136) Ding, S. Y.; Yi, J.; Li, J.-F.; Ren, B.; Wu, D.-Y.; Panneerselvam, R.; Tian, Z.-Q. *Nat. Rev. Mater.* **2016**, *1* (6), 16021.
- (137) Wang, C.; Yu, Y.; Irfan, M.; Xu, B.; Li, J.; Zhang, L.; Qin, Z.; Yu, C.; Liu, H.; Su, X. *Small* **2020**, *16* (44), 2002578.
- (138) Lee, Y.; Kim, D.-H. *Nat. Biomed.* **2019**, *3* (1), 5–6.
- (139) Bu, Y.; Zhu, X.; Wang, H.; Zhang, J.; Wang, L.; Yu, Z.; Tian, Y.; Zhou, H.; Xie, Y. *Anal. Chem.* **2021**, *93* (35), 12059–12066.
- (140) Liu, J.; Zheng, T.; Tian, Y. *Angew. Chem., Int. Ed.* **2019**, *58* (23), 7757–7761.
- (141) Zhu, W.; Gao, M. Y.; Zhu, Q.; Chi, B.; Zeng, L.-W.; Hu, J.-M.; Shen, A.-G. *Nanoscale* **2020**, *12* (5), 3292–3301.
- (142) Wang, J.; Sun, J.; Wang, Y.; Chou, T.; Zhang, Q.; Zhang, B.; Ren, L.; Wang, H. *Adv. Funct. Mater.* **2020**, *30* (9), 1908825.
- (143) Nayak, T. R.; Andreou, C.; Oseledchik, A.; Marcus, W. D.; Wong, H. C.; Massagué, J.; Kircher, M. F. *Nanoscale* **2017**, *9* (3), 1110–1119.
- (144) Yue, Q.; Gao, X.; Yu, Y.; Li, Y.; Hua, W.; Fan, K.; Zhang, R.; Qian, J.; Chen, L.; Li, C.; Mao, Y. *Nanoscale* **2017**, *9* (23), 7930–7940.
- (145) Han, L.; Duan, W.; Li, X.; Wang, C.; Jin, Z.; Zhai, Y.; Cao, C.; Chen, L.; Xu, W.; Liu, Y.; Bi, Y. Y.; Feng, J.; Mao, Y.; Yue, Q.; Zhang, X. Y.; Li, C. *ACS Appl. Mater. Interfaces* **2019**, *11* (17), 15241–15250.
- (146) Shi, B.; Zhang, B.; Zhang, Y.; Gu, Y.; Zheng, C.; Yan, J.; Chen, W.; Yan, F.; Ye, J.; Zhang, H. *Acta Biomater.* **2020**, *104*, 210–220.
- (147) Zhang, Y.; Qiu, Y.; Lin, L.; Gu, H.; Xiao, Z.; Ye, J. *ACS Appl. Mater. Interfaces* **2017**, *9* (4), 3995–4005.
- (148) Li, J.-F.; Zhang, Y. J.; Ding, S. Y.; Panneerselvam, R.; Tian, Z. Q. *Chem. Rev.* **2017**, *117* (7), 5002–5069.
- (149) Yang, W.; Lim, D.-K. *Adv. Mater.* **2020**, *32* (51), 2002219.
- (150) Wei, Q.; Arami, H.; Santos, H. A.; Zhang, H.; Li, Y.; He, J.; Zhong, D.; Ling, D.; Zhou, M. *Adv. Sci.* **2021**, *8* (5), 2002788.



JACS Au
AN OPEN ACCESS JOURNAL OF THE AMERICAN CHEMICAL SOCIETY

 Editor-in-Chief
Prof. Christopher W. Jones
Georgia Institute of Technology, USA

Open for Submissions 

pubs.acs.org/jacsau  ACS Publications
Most Trusted. Most Cited. Most Read.